© 2022. Published by The Company of Biologists Ltd | Journal of Cell Science (2022) 135, jcs258969. doi:10.1242/jcs.258969

RESEARCH ARTICLE

Emerin self-assembly and nucleoskeletal coupling regulate nuclear envelope mechanics against stress

Anthony Fernandez[1], Markville Bautista[2], Liying Wu[1] and Fabien Pinaud[1,2,3,*]

ABSTRACT

Emerin is an integral nuclear envelope protein that participates in the maintenance of nuclear shape. When mutated or absent, emerin causes X-linked Emery-Dreifuss muscular dystrophy (EDMD). To understand how emerin takes part in molecular scaffolding at the nuclear envelope and helps protect the nucleus against mechanical stress, we established its nanoscale organization using single-molecule tracking and super-resolution microscopy. We show that emerin monomers form localized oligomeric nanoclusters stabilized by both lamin A/C and the SUN1-containing linker of nucleoskeleton and cytoskeleton (LINC) complex. Interactions of emerin with nuclear actin and BAF (also known as BANF1) additionally modulate its membrane mobility and its ability to oligomerize. In nuclei subjected to mechanical challenges, the mechanotransduction functions of emerin are coupled to changes in its oligomeric state, and the incremental self-assembly of emerin determines nuclear shape adaptation against mechanical forces. We also show that the abnormal nuclear envelope deformations induced by EDMD emerin mutants stem from improper formation of lamin A/C and LINC complex-stabilized emerin oligomers. These findings place emerin at the center of the molecular processes that regulate nuclear shape remodeling in response to mechanical challenges.

KEY WORDS: Laminopathy, Super-resolution microscopy, Mechanobiology, Nuclear envelope, Emerin

INTRODUCTION

Emerin is an inner nuclear membrane (INM) protein that participates in the maintenance of the nuclear architecture by interacting with the lamina and elements of the linker of nucleoskeleton and cytoskeleton (LINC) complex (Berk et al., 2013b; Kirby and Lammerding, 2018). Emerin also contributes to tethering chromatin at the nuclear envelope (NE) by binding the DNA-bridging barrier-to-autointegration factor (BAF, also known as BANF1) and regulating the activity of chromatin compaction modulators (Cui et al., 2015; Demmerle et al., 2012). Both the nucleoskeleton and the compaction state of chromatin contribute to the mechanical responses of nuclei, and emerin is deemed a pivotal actor of mechanotransduction processes at the NE (Maurer and Lammerding, 2019). When mutated or absent, emerin causes X-linked Emery-Dreifuss muscular dystrophy (EDMD), a disease that is part of a larger group of laminopathies associated with structural perturbations of the NE and its underlying lamina (Emery and Dreifuss, 1966). Although emerin is ubiquitously expressed, mutations in the *EMD* gene primarily affect cells exposed to extensive mechanical stress, such as skeletal and cardiac muscle cells. Emerin-null muscle tissues display deformed and disorganized nuclei, impaired myogenesis and improper muscle fiber formation, which participate in the muscle wasting and cardiac disease phenotypes of EDMD (Fidzianska and Hausmanowa-Petrusewicz, 2003). In non-muscle cells, loss of emerin also leads to altered NE elasticity and increased nuclear fragility (Rowat et al., 2006), impaired expression of mechanosensitive genes and enhanced apoptosis after mechanical strain (Lammerding et al., 2005). These EDMD phenotypes likely stem from both an altered structural integrity of the NE and modified gene expression profiles.

The structure of emerin and its binding to various partners have been extensively characterized (Berk et al., 2013b). Emerin is 254 amino acids (aa) long, with an N-terminal globular LAP2-emerin-MAN1 domain (LEM, aa:1-45), followed by a long intrinsically disordered region (IDR, aa:46-222) and a C-terminal transmembrane domain (aa:223-234) that allows anchoring to the NE. Prominent binding partners of emerin include lamin A/C and lamin B (Clements et al., 2000; Sakaki et al., 2001), actin (Fairley et al., 1999), BAF (Lee et al., 2001), nesprins and SUN proteins from the LINC complex (Haque et al., 2010; Mislow et al., 2002) and other factors (Berk et al., 2013b). While emerin binds to BAF via its LEM domain, its interactions with other binding partners and self-association are mediated by the IDR (Berk et al., 2014; Herrada et al., 2015). Emerin monomers can oligomerize via IDR segments that serve as LEM binding and self-assembly sites, and *in vitro*, emerin self-association into filamentous structures impacts its interactions with lamin A/C and BAF (Berk et al., 2014; Samson et al., 2017). Post-translational modifications of emerin also influence its oligomerization and its interactions with binding partners (Berk et al., 2013a; Roberts et al., 2006). In isolated nuclei, phosphorylation of emerin residues Y74 and Y95 are required for lamin A/C recruitment to the LINC complex and NE stiffening in response to mechanical loads (Guilluy et al., 2014). Additional post-translational modifications regulate the affinity of the LEM domain for BAF (Berk et al., 2013a) and binding to actin (Hirano et al., 2005). However, how emerin organizes at the NE and participates in protecting the nucleus against mechanical strain remains unclear.

EDMD is often caused by frame-shift deletions and nonsense mutations that effectively ablate emerin expression in cells. Yet, a few sets of point mutations and deletions, including Δ95-99, Q133H and P183H/T, also cause EDMD despite normal cellular expression levels of these emerin mutants and their localization at the NE (Fairley et al., 1999; Holt et al., 2001). These mutants display altered self-association and binding to nucleoskeletal proteins *in vitro* (Berk et al., 2013b; Herrada et al., 2015) and possible changes to their

[1]Department of Biological Sciences, University of Southern California, 1050 Childs Way, Los Angeles, CA 90089, USA. [2]Department of Chemistry, University of Southern California, 1050 Childs Way, Los Angeles, CA 90089, USA. [3]Department of Physics and Astronomy, University of Southern California, 1050 Childs Way, Los Angeles, CA 90089, USA.

*Author for correspondence (pinaud@usc.edu)

F.P., 0000-0002-4272-3616

Handling Editor: Jennifer Lippincott-Schwartz
Received 27 May 2021; Accepted 14 February 2022

Journal of Cell Science (2022) 135, jcs258969. doi:10.1242/jcs.258969

molecular organization at the NE might explain how they induce EDMD.

Here, we performed super-resolution imaging by using direct stochastic optical reconstruction microscopy (dSTORM) (van de Linde et al., 2011) and single-particle tracking via photoactivated localization microscopy (sptPALM) (Subach et al., 2010) to investigate the nanoscale organization of wild-type and mutant emerin in cells. By modulating the mechanical landscape of nuclei using cell micropatterning techniques (Fernandez et al., 2017), we also studied how emerin participates in NE mechanotransduction processes during stress. We show that emerin oligomerization and its differential interactions with key structural partners at the NE is central to nuclear shape adaptation against mechanical challenges.

RESULTS

Emerin displays distinct diffusive behaviors at the nuclear envelope

To study the NE dynamics of wild-type and dystrophy-causing mutations of emerin, emerin proteins fused to photoactivable red fluorescent protein (PA-TagRFP–emerin) were expressed in emerin-null human dermal fibroblasts (HDFs) from an EDMD patient ($EMD^{-/y}$). PA-TagRFP–emerin expression led to its expected localization at the NE, as observed for endogenous emerin in HDFs from a healthy individual ($EMD^{+/y}$) (Fig. 1A). Upon re-expression of wild-type emerin fusions in $EMD^{-/y}$ HDFs, nuclear deformations against mechanical stress were previously found to recover to levels similar to wild-type $EMD^{+/y}$ HDFs (Bautista et al., 2019). For sptPALM, we imaged individual PA-TagRFP–emerin molecules using highly inclined and laminated optical sheet excitation at the ventral NE (Tokunaga et al., 2008). Diffusion tracks were generated from localized emerin appearances (Fig. 1B; Movie 1) and analyses were performed using the probability distribution of square displacements (PDSDs) (Schutz et al., 1997) to separate unique diffusive behaviors (Fig. 1C).

We observed that wild-type emerin exhibited four distinct diffusive behaviors with diffusion coefficients D_1, $2.21\times10^{-1}\pm4.9\times10^{-2}$ μm^2 s^{-1}, a value similar to that reported for endoplasmic reticulum (ER) membrane diffusion (Ostlund et al., 1999); D_2, $1.48\times10^{-2}\pm1.5\times10^{-3}$ μm^2 s^{-1}, D_3, $1.73\times10^{-3}\pm1.1\times10^{-4}$ μm^2 s^{-1}; and D_4, $2.6\times10^{-4}\pm1\times10^{-5}$ μm^2 s^{-1} (mean±s.e.m.) (Fig. 1D; Table S1). The population D_1 represented 1% of the detected behaviors, whereas population D_2 represented 9%, a small emerin fraction comparable to that expected at the outer nuclear membrane (ONM) (Salpingidou et al., 2007). The two slowest populations D_3 and D_4 collectively represented 90% of total emerin diffusive behaviors. Based on their individual diffusion coefficients, we grouped emerin trajectories into four diffusion ranges and plotted them as maps. In trajectory maps, the fastest emerin population D_1 primarily distributed in the vicinity of the NE, consistent with diffusion in the ER membrane, whereas the three slower populations D_2-D_4 were enriched at the NE (Fig. 1E). Compared to measurements by fluorescence recovery after photobleaching (FRAP), where only two diffusive behaviors of emerin were detected (Fig. S1), sptPALM revealed that emerin has four distinct types of diffusions.

Emerin organizes as slowly diffusing monomers or oligomers at the inner nuclear membrane

Although emerin primarily localizes at the INM, it is often detected at the ONM, where it does not interact with the nuclear lamina (Salpingidou et al., 2007). To assess whether the diffusing population D_2 corresponded to ONM-associated emerin, sptPALM was performed after lamin A/C depletion by siRNA (Fig. S2). Downregulating the expression of lamin A/C did not affect emerin populations D_1 and D_2 (not significant, Fig. 2A) but the mobility of populations D_3 (40%) and D_4 (50%) increased ($P<0.01$, Fig. 2A; Table S1), consistent with their localization at the INM and with population D_2 diffusing at the ONM. In accordance with the majority of emerin being distributed as two distinct INM pools, depletion of nuclear actin by downregulating the expression of the actin nuclear import factor importin-9 (Dopie et al., 2012) (IPO9, Figs S2, S3) also resulted in the increased mobility of populations D_3 and D_4, although faster emerin diffusion at the ONM was also observed (Fig. 2A; Table S1). The 9% fraction of emerin diffusing at the ONM agreed well with quantitative immunostaining measurements (Fig. S4), indicating that 13±6% (mean±s.d.) of the emerin pool localizes at the ONM in $EMD^{+/y}$ HDFs (Fig. S4).

Emerin can self-assemble *in vitro*, which might explain its slow INM mobility if emerin oligomers are tethered by the nucleoskeleton. To determine whether diffusing populations D_3 or D_4 correspond to emerin monomers or oligomers, we coexpressed wild-type emerin fused to self-complementary split-GFP fragments (Fig. 2B), induced the formation of complemented emerin–GFP–emerin species and tracked their mobility by complementation activated light microscopy (CALM) (Pinaud and Dahan, 2011). We found that emerin–GFP–emerin species localized almost exclusively at the NE (Fig. 2C; Movie 2), with 90% diffusing like population D_4 (not significant, Fig. 2D) and 10% diffusing like the ONM population D_2 (not significant, Fig. 2D). Fluorescent species with mobilities matching those of the ER population D_1 or the INM population D_3 were not detected. Emerin–GFP–emerin trajectories often spatially overlapped, suggesting that emerin forms multimers rather than strictly dimers at the INM (Fig. 2C). This indicates that population D_3 detected by sptPALM but not by CALM represents emerin monomers, whereas the slowest population D_4 represents INM emerin oligomers, as subsequently confirmed by super-resolution imaging (Fig. 3). The detection of a few emerin–GFP–emerin species at the ONM is likely due to split-GFP-induced emerin dimers that cannot translocate through peripheral nuclear pore channels and do not access the INM.

BAF binding modulates the mobility of both emerin monomers and oligomers distributed across the INM

BAF binds the LEM domain of emerin with high affinity and could participate in the slow INM diffusion of emerin via its additional interactions with lamin A/C (Samson et al., 2018) and chromatin (Burger et al., 2020). To study how binding of emerin to BAF influences its mobility, endogenous BAF was depleted by using siRNA (Fig. S2) and replaced by the expression of BAF^{L58R}, a mutant that does not bind LEM domains but binds lamin A/C and chromatin (Samwer et al., 2017). When unable to bind BAF^{L58R}, emerin monomers and oligomers diffused significantly faster at the INM, with lateral mobilities higher than for lamin A/C or IPO9 knockdown ($P<0.01$, Fig. 2A; Table S1). Although emerin diffusion at the ER was undisturbed, its mobility at the ONM increased ($P<0.01$, Fig. 2A), suggesting that cytoplasmic BAF also interacts with emerin at the ONM. Given that BAF is highly mobile in the nucleus (Shimi et al., 2004), the comparatively slow mobility of BAF-bound emerin likely stems from the formation of ternary complexes with lamin A/C or chromatin. As knockdown of endogenous BAF and expression of BAF^{L58R} did not alter the expression of lamin A/C nor its nuclear localization (Fig. S2), the stronger influence of BAF^{L58R} on emerin dynamics as compared to

Journal of Cell Science (2022) 135, jcs258969. doi:10.1242/jcs.258969

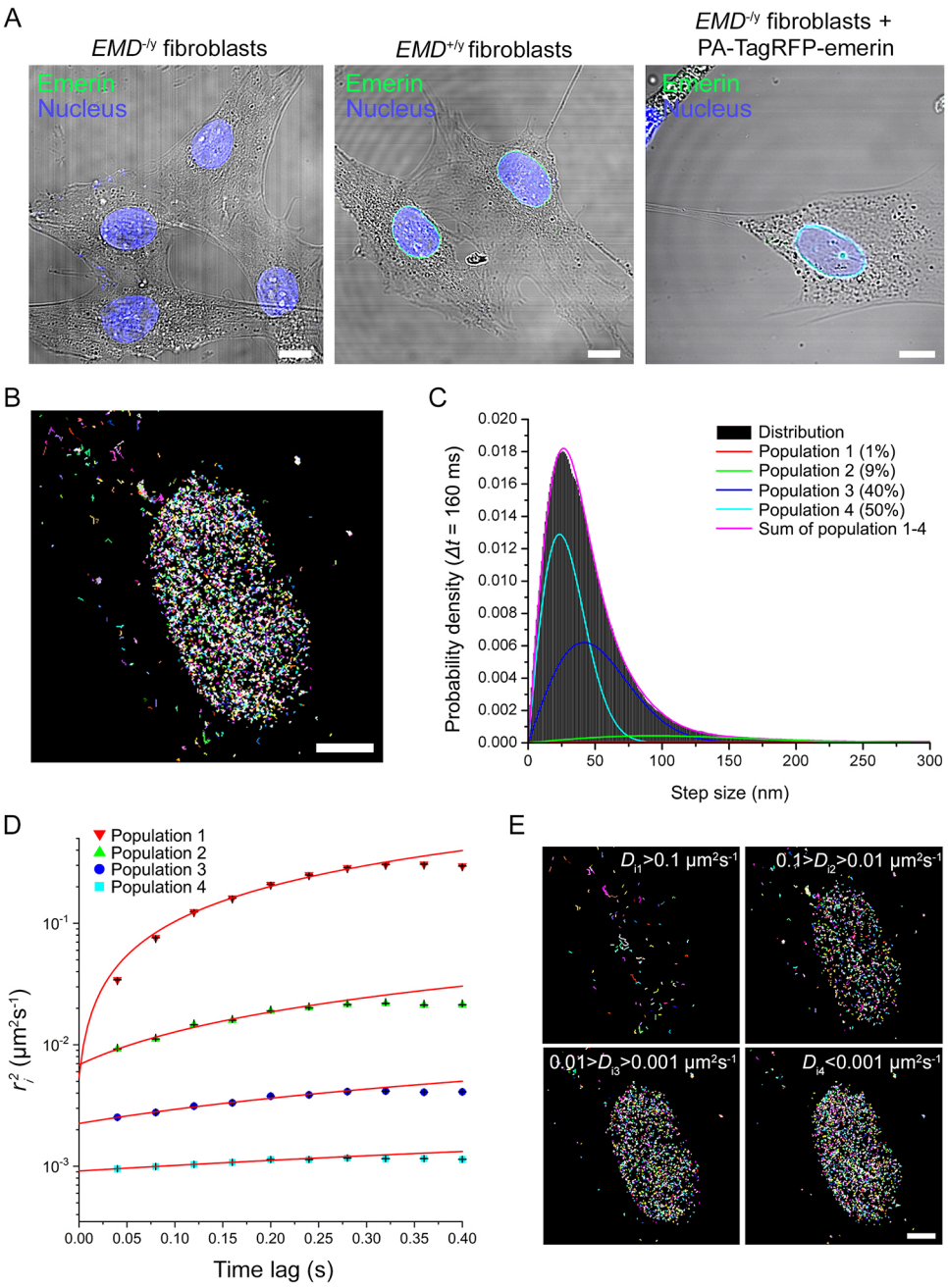

Fig. 1. Emerin displays distinct diffusive behaviors at the nuclear envelope. (A) Confocal imaging of emerin (green) in *EMD*$^{-/y}$ HDFs, *EMD*$^{+/y}$ HDFs and *EMD*$^{-/y}$ HDFs expressing wild-type PA-TagRFP–emerin. The nucleus is shown in blue. Scale bars: 10 µm. (B) Trajectory map of individual PA-TagRFP–emerin in a single cell. Scale bar: 5 µm. (C) Probability distribution of square displacements for wild-type emerin at time lag Δt=160 ms. (D) Square displacement curves (r^2_i) of each emerin diffusive behavior fitted over the first four values with a Brownian diffusion model (red line). (E) Emerin trajectory maps as a function of individual diffusion coefficient (D_i). Images are representative of 14 cell nuclei. Scale bar: 5 µm.

lamin A/C depletion indicates that BAF not only modulates the mobility of emerin via ternary binding to lamin A/C, but also via additional interactions with other nuclear components, potentially chromatin.

The global influence of BAF and the nucleoskeleton on the mobility of emerin was also captured in diffusion maps built by spatial rendering of diffusion coefficients at the position of each tracked PA-TagRFP–emerin (Fig. 2E). In these maps, slow diffusion domains attributed to emerin oligomers were distributed throughout the NE and were surrounded by areas where the mobility of emerin was faster, as expected for monomers (Fig. 2E). This indicates a membrane-wide, yet locally structured, distribution of emerin, with monomers surrounding oligomer domains, consistent with emerin monomer–oligomer exchanges in distinct INM areas. Together, these results show that emerin diffuses rapidly at the ER membrane on its way to the juxtaposed ONM, where its diffusion is slower, in part by its interaction with cytoplasmic BAF. Once at the INM, the mobility of emerin is further reduced, with monomers and oligomers interacting with nuclear BAF and the nucleoskeleton, consistent with a combined BAF-induced and lamina-induced retention of emerin at the INM.

Emerin forms discrete oligomeric nanodomains surrounded by monomers

We then probed the organization of emerin in greater detail using super-resolution microscopy. Wild-type emerin fused to a SNAP-tag was expressed in *EMD*$^{-/y}$ HDFs and imaged at the ventral NE by dSTORM with benzylguanine-Alexa Fluor 647 (Fig. 3A). Emerin neighborhood density functions (NDFs) built from localized emerin positions were compared to Monte Carlo simulations of completely random distributions and fitted to measure molecular densities and length scales of significant clustering. We found that wild-type

Journal of Cell Science (2022) 135, jcs258969. doi:10.1242/jcs.258969

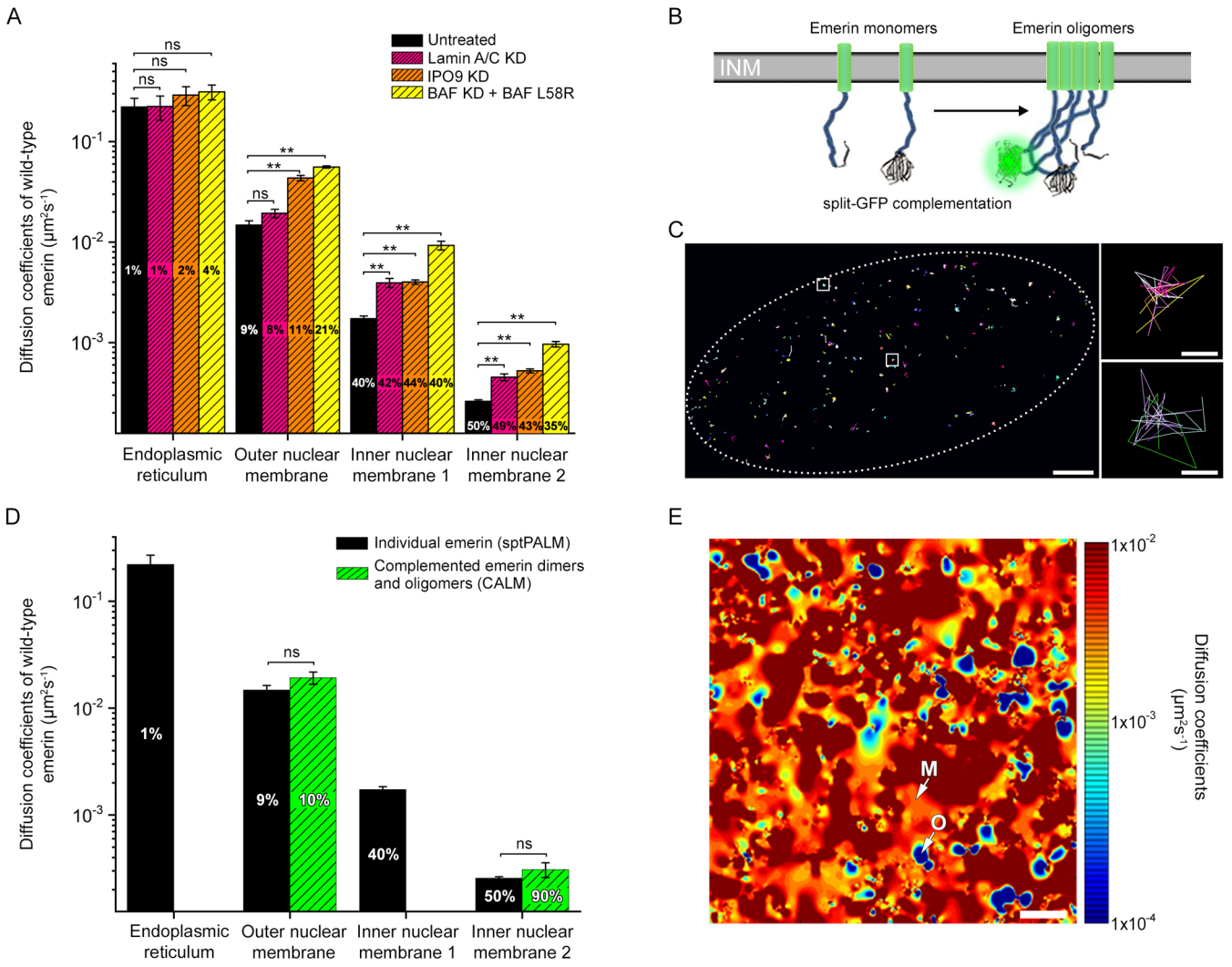

Fig. 2. Emerin diffuses as monomers and oligomers interacting with lamin A/C, nuclear actin and BAF. (A) Diffusion coefficients (mean±s.e.m.) and percentages of wild-type emerin after lamin A/C depletion, nuclear actin depletion (IPO9 knockdown) or replacement of endogenous BAF with BAF^{L58R}. (B) Schematic of emerin fusion to complementary split-GFP fragments. (C) Trajectory map of complemented emerin–GFP–emerin at the NE. Squares: oligomeric nanodomains with overlapping trajectories. Scale bars: 2 µm (left) and 50 nm (right). (D) Diffusion coefficients (mean±s.e.m.) and percentages for wild-type emerin assessed by sptPALM and complemented emerin–GFP–emerin species assessed by CALM. (E) Diffusion map of wild-type PA-TagRFP–emerin, showing slow mobility oligomeric domains (blue, O) surrounded by areas where emerin monomers diffuse faster (red, M). Scale bar: 500 nm. Sample sizes (*n*) for A and D are provided in the Materials and Methods. Images in C,E are representative of 13 and 14 cell nuclei, respectively. ***P*<0.01; ns, not significant (two-tailed unpaired *t*-test).

emerin was not distributed randomly at the NE, as it displayed density distributions significantly higher than expected for a completely random organization (Fig. 3B). NDFs were best fitted with a two-exponential decay model, indicating that emerin organizes into two distinct clustering states across the NE. The first clusters had typical sizes of 22±11 nm (mean±s.e.m.) and molecular densities of emerin 8.2±0.2-fold higher than expected for a random distribution (Fig. 3C; Table S2). The second clusters were significantly larger with typical sizes of 236±30 nm and emerin densities slightly above the expected value of 1 for complete randomness (1.3±0.1-fold, Fig. 3C). In local cluster maps, emerin formed small high-density clusters bordered by larger NE areas with emerin densities close to random (Fig. 3D). Those distributions were similar to sptPALM diffusion maps, and corroborate that emerin organizes into discrete oligomers surrounded by dispersed emerin monomers across the INM. A similar organization of emerin was observed at the dorsal NE (Fig. S5). While it is intriguing that emerin monomers appear slightly clustered, their completely random distribution was not expected because they do not populate membrane-less areas of the NE, such as nuclear pores.

Emerin oligomers are stabilized by lamin A/C and SUN1-containing LINC complexes, and are modulated by nuclear actin and BAF

We then determined how lamin A/C, nuclear actin, BAF and SUN1 from the LINC complex participate in the spatial organization of emerin at the INM. Wild-type emerin was imaged by dSTORM after siRNA knockdown of lamin A/C, IPO9 or SUN1, or replacement of endogenous BAF with BAF^{L58R}. After lamin A/C depletion, the molecular density of emerin was reduced (Fig. 3B), and emerin distributed into 35±17 nm (mean±s.e.m.) nanodomains with densities close to random (1.2±0.1-fold, Fig. 3C; Table S2) and into large 950±173 nm monomer domains with densities just above random (1.1±0.1-fold, Fig. 3C). Compared to controls, emerin monomers were dispersed over larger areas and oligomers nearly vanished, as seen in emerin cluster maps of lamin A/C-depleted

Journal of Cell Science (2022) 135, jcs258969. doi:10.1242/jcs.258969

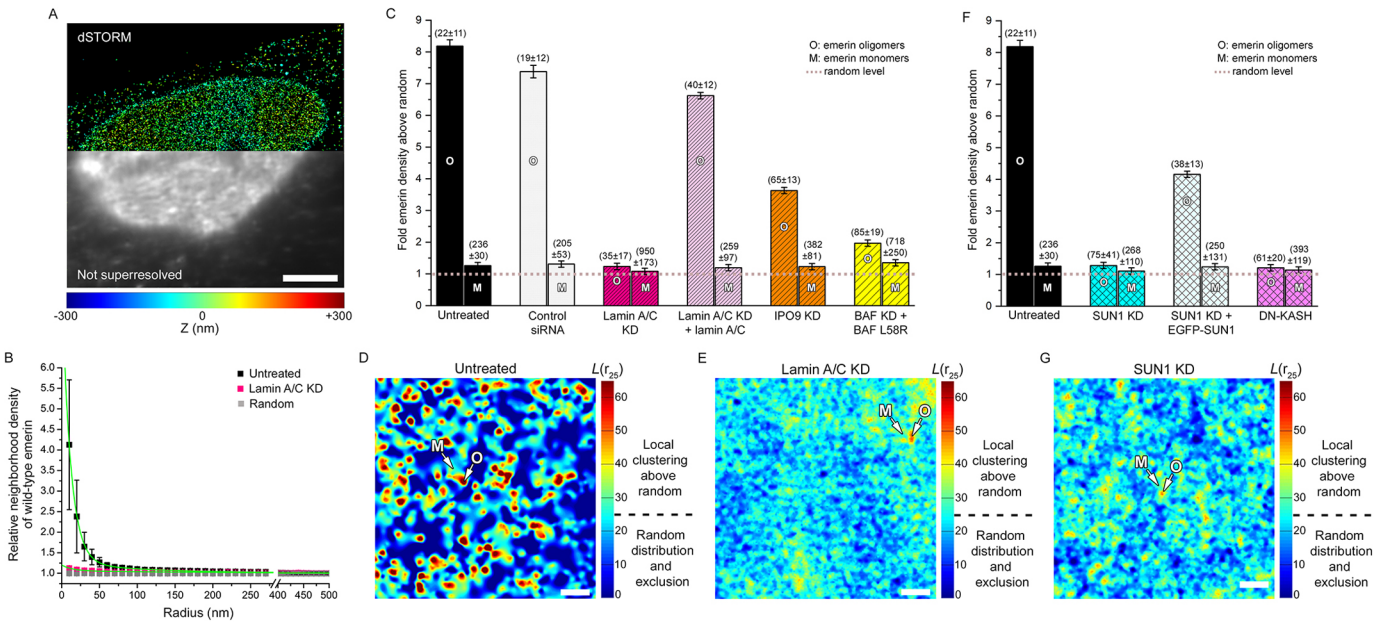

Fig. 3. Emerin forms oligomeric nanodomains stabilized by lamin A/C and SUN1 at the LINC complex. (A) Super-resolved (top) and diffraction-limited imaging (bottom) of wild-type SNAP–emerin. Scale bar: 5 µm. (B) Neighborhood densities (mean±s.d.) at various length scales for wild-type emerin before and after lamin A/C knockdown, compared to complete spatial randomness. Fit shown in green. (C) Molecular densities above random (mean±s.e.m.) of wild-type emerin oligomers (O) and monomers (M) in untreated cells, after control siRNA, lamin A/C knockdown (KD), lamin A/C knockdown and exogenous expression of lamin A/C, IPO9 knockdown to deplete nuclear actin or replacement of endogenous BAF by BAF^{L58R}. Values in parentheses represent the size (mean±s.e.m.) of each domain in nanometers. (D) Local cluster map of wild-type emerin at the NE of an untreated HDF. (E) Local cluster map of wild-type emerin after lamin A/C knockdown. (F) Molecular densities above random (mean±s.e.m.) for wild-type emerin in untreated cells, after SUN1 knockdown, after SUN1 knockdown and exogenous expression of EGFP-SUN1 or after exogenous expression of mCherry-DN-KASH. (G) Local cluster map of wild-type emerin after SUN1 knockdown. For D, E, G: M, monomer areas; O, oligomer nanodomains. Scale bars: 250 nm. Sample sizes (*n*) in B, C and F are provided in the Materials and Methods. Images in A, D, E and G are representative of 10, 10, 6 and 6 cell nuclei, respectively.

nuclei (Fig. 3E). The spatial distribution of emerin and oligomerization returned to near normal levels upon exogenous expression of an siRNA-resistant lamin A/C (Fig. 3C; Fig. S6), but overexpression induced a loss of emerin oligomers (Fig. S6), indicating that balanced levels of lamin A/C are essential to promote emerin self-assemblies. Although lamin A/C depletion indirectly led to decreased nuclear actin levels (Fig. S2), emerin oligomers were not as severely disrupted when nuclear actin was specifically depleted, as we show next (see Fig. 3C). These results indicate that lamin A/C plays a central role in the formation and stabilization of emerin oligomers, and additionally influences the spatial distribution of emerin monomers at the INM.

When nuclear actin was depleted after IPO9 knockdown, emerin formed oligomers with reduced molecular densities of 3.6±0.1-fold above random and sizes of 65±13 nm (Fig. 3C; Table S2). Emerin monomers were dispersed over 382±81 nm domains, which were larger than in untreated cells (236±30 nm, Fig. 3C), but not as large as for lamin A/C depletion (950±173 nm, Fig. 3C). Thus, despite reduced nuclear actin levels, emerin still oligomerized but redistributed over broader INM domains. Conversely, nuclear accumulation of actin upon siRNA-mediated knockdown of exportin 6 (XPO6, Fig. S3) did not affect the organization of emerin monomers, but oligomer densities decreased to 1.5±0.1-fold above random in 49±16 nm nanodomains (Fig. S7), suggesting that excess nuclear actin impedes the formation of dense emerin oligomers. Thus, together with lamin A/C, nuclear actin contributes to the spatial organization of emerin at the INM and participates in the maintenance of emerin oligomers.

When endogenous BAF was replaced by BAF^{L58R}, emerin oligomers still formed but with reduced molecular densities of 2.0±0.1-fold above random and larger sizes of 85±19 nm compared to those in control cells (Fig. 3C; Table S2). The inability to bind BAF also induced a redistribution of emerin monomers over large INM domains with typical sizes of 718±250 nm (Fig. 3C). Hence, and consistent with our diffusion results, emerin binding to BAF modulates the organization of both oligomeric and monomeric emerin and strongly influences the spatial distribution of emerin monomers at the INM.

When SUN1 was depleted to destabilize SUN1-containing LINC complexes (Fig. S2), the formation of emerin oligomers was reduced to levels equivalent to those seen upon lamin A/C depletion. Emerin distributed over 75±41 nm nanodomains with molecular densities decreased to 1.2±0.1-fold above random (Fig. 3F; Table S2), and over NE areas with sizes of 268±110 nm, similar to the spatial distribution of emerin monomers in untreated cells (Fig. 3F). This indicates that reduced SUN1 expression levels primarily influence the formation of emerin oligomers at the INM. In cluster maps, depletion of SUN1 effectively resulted in a largely random distribution of emerin and, like for lamin A/C depletion, few emerin clusters were visible (Fig. 3G). This loss of emerin oligomers was partially rescued upon expression of an exogenous and siRNA-resistant EGFP-SUN1 (Fig. 3F; Fig. S6), but overexpression induced a mis-localization of both EGFP-SUN1 and emerin from the NE (Fig. S6), and a concomitant reduction in emerin oligomerization (Fig. S6), indicating that, as for lamin A/C, a balanced cellular expression of SUN1 is required for the self-assembly of emerin at the INM. Although SUN1 interacts with lamin A (Crisp et al., 2006; Haque et al., 2006), the expression and NE localization of lamin A/C was not disrupted upon SUN1 knockdown and, reciprocally, lamin A/C depletion did not modify the expression of SUN1 nor its distribution at the NE (Fig. S2).

Journal of Cell Science (2022) 135, jcs258969. doi:10.1242/jcs.258969

Thus, together with lamin A/C, a regulated expression of SUN1 is required for the formation of emerin oligomers and their localized distribution at the INM. SUN1 itself has been shown to self-assemble into nearly immobile platforms that can serve as sites for macromolecular assemblies at LINC complexes (Hennen et al., 2018; Lu et al., 2008). To assess whether emerin locally oligomerized at LINC complexes, we expressed a dominant-negative KASH domain from nesprin-1α (mCherry-DN-KASH) (Lombardi et al., 2011), which disrupts LINC complexes by binding to SUN proteins and impeding their interaction with endogenous KASH domain proteins at the NE. In cells expressing mCherry-DN-KASH, emerin oligomers were disrupted at levels equivalent to those seen with SUN1 siRNA (Fig. 3F; Table S2), indicating that the oligomerization of emerin requires functional SUN–nesprin interactions and a coupling of the nucleoskeleton and the cytoskeleton via SUN1-containing LINC complexes.

Together, these results show that emerin monomers are distributed across the INM where their distribution is modulated by direct binding to BAF and additional spatial constraints imposed by lamin A/C and nuclear actin. Emerin also self-assembles into discrete and small oligomeric nanodomains that are structurally costabilized by lamin A/C and SUN1 from the LINC complex, and are maintained, to a lesser extent, by BAF and nuclear actin.

Increased diffusion and oligomerization of emerin upon nuclear adaptation to mechanical stress

We then studied how the mobility and organization of emerin are affected in nuclei subjected to increasing mechanical stress. SptPALM and super-resolution imaging of wild-type emerin were performed in *EMD*$^{-/y}$ HDFs grown on increasingly narrow rectangular micropatterns with widths from 15 µm to 5 µm to impose steady-state mechanical stress to the nucleus (Fig. 4A,B) and increase mechanical load at LINC complexes (Arsenovic et al., 2016). First, we verified that changes in nuclear shape index (NSI) on these micropatterns reflect the mechanical adaptation of nuclei against mechanical forces by depleting lamin A/C or nuclear actin, two key nucleoskeletal proteins involved in maintaining nuclear shape. In non-patterned cells, we found that nuclei were less circular after lamin A/C or nuclear actin depletion compared to control cells (P<0.01, Fig. 4C). These effects were amplified on micropatterns where nuclei became increasingly deformed as the patterns got narrower (P<0.01, Fig. 4C), indicating that cell micropatterning elicits increased nuclear stress and effectively induces mechanical responses that implicate the nucleoskeleton.

When we tracked wild-type PA-TagRFP–emerin on deformed nuclei in 15 µm and 10 µm patterns (Movie 3), we found that its ER mobility was unchanged compared to non-patterned cells (not significant, Fig. 4D; Table S1), whereas it diffused faster at the ONM (P<0.01, Fig. 4D). At the INM, emerin monomers also diffused significantly faster (P<0.01, Fig. 4D) and the mobility of oligomers increased, albeit short of statistical significance for 15 µm patterns (not significant and P<0.01, Fig. 4D). Interestingly, there were no significant differences in the mobilities of all four ER, ONM, INM monomer and INM oligomer emerin populations on both types of micropatterns compared to nuclear actin depletion (not significant, Fig. S8), suggesting that nuclear shape adaptation to mechanical cues involves modified interactions of emerin with nuclear actin, notably for monomers.

Spatial distribution analyses further indicated that as the NSI decreased, emerin monomers dispersed over increasingly large INM domains with sizes of 382±62 nm and 460±136 nm, compared to 236±30 nm for non-stressed nuclei (Fig. 4E). Concurrently, oligomer densities dropped from 8.2±0.2-fold to 3.6±0.1-fold above random in 15 µm patterns, before increasing to 4.6±0.1-fold above random in 10 µm patterns (Fig. 4E). Remarkably, oligomeric nanodomains became larger during nuclear stress and their sizes expanded from 22±11 nm to 60±13 nm in both micropatterns (Fig. 4E). When considering this wider spatial distribution, the relative oligomerization of emerin in deformed nuclei compared to non-deformed nuclei increased by 3.4-fold and by 4.1-fold as the nucleus adapted to incremental mechanical stress (Fig. 4F). This shows that nuclear shape adaptation to forces is associated with a gradual change in the oligomerization potential of emerin at the INM. This increased self-assembly of emerin over larger nanodomains was accompanied by a faster lateral mobility of emerin and appeared to be triggered by nucleoskeletal rearrangements. Indeed, the stress-induced spatial reorganization of emerin in micropatterns, including oligomer densities and emerin domain sizes, were analogous to those seen when nuclear actin is depleted in non-patterned cells (Fig. S8; Table S2). Consistent with the contribution of nuclear actin to changes in nuclear volume (Baarlink et al., 2017), these observations suggest that nuclear shape deformation involves a disengagement of nuclear actin from the nucleoskeleton that results in faster emerin diffusion and increased oligomerization. Increased lateral mobilities of emerin at the INM could indeed facilitate molecular collisions between monomers and the formation of oligomers that are stabilized by lamin A/C and SUN1 at LINC complexes. These results indicate that the mechanotransduction functions of emerin are coupled to changes in its oligomeric state along the INM and are modulated by emerin interactions with nucleoskeletal partners, including nuclear actin, to ensure appropriate nuclear deformation and response to mechanical challenges.

Emerin mutants induce abnormal nuclear deformation against mechanical stress

To further establish the significance of emerin oligomerization for nuclear adaptation to mechanical stress, we then compared the organization of wild-type emerin to that of mutated forms of emerin known to induce EDMD. We studied how mutation Q133H, deletion Δ95-99 and mutation P183H (Fig. 5A) affect the diffusion and the nanoscale distribution of emerin at the NE. First, we verified that these emerin mutants could effectively induce defective mechanical responses of nuclei when expressed in *EMD*$^{-/y}$ HDFs by comparing changes in NSI after random cell plating or plating on increasingly narrow micropatterns (Fig. 5B,C). In randomly plated cells, the expression of mutated emerin resulted in slightly less circular nuclei compared to those seen in cells expressing wild-type emerin (Fig. 5B). With increasing mechanical stress, cells expressing emerin mutants displayed significantly higher NSI than cells expressing wild-type emerin (Fig. 5B), indicative of a failure to correctly modify the shape of the nucleus in response to mechanical forces. These deficient changes in nuclear shape were accompanied by a mispositioning of the nucleus relative to the cell major axis, nuclear crumpling, abnormal organization of the actin cytoskeleton and failure of cells to properly fit within micropatterns, specifically in cell areas adjacent to the misshaped nucleus (Fig. 5C). This indicates that the expression of mutated emerin in *EMD*$^{-/y}$ HDFs effectively impedes nuclear adaptation to mechanical stress.

Emerin mutants display defective oligomerization at the INM

Q133H mutation

We then characterized the NE dynamics of each emerin mutant and their respective nanoscale organization, starting with Q133H emerin. We found that the lateral mobility of Q133H

Journal of Cell Science (2022) 135, jcs258969. doi:10.1242/jcs.258969

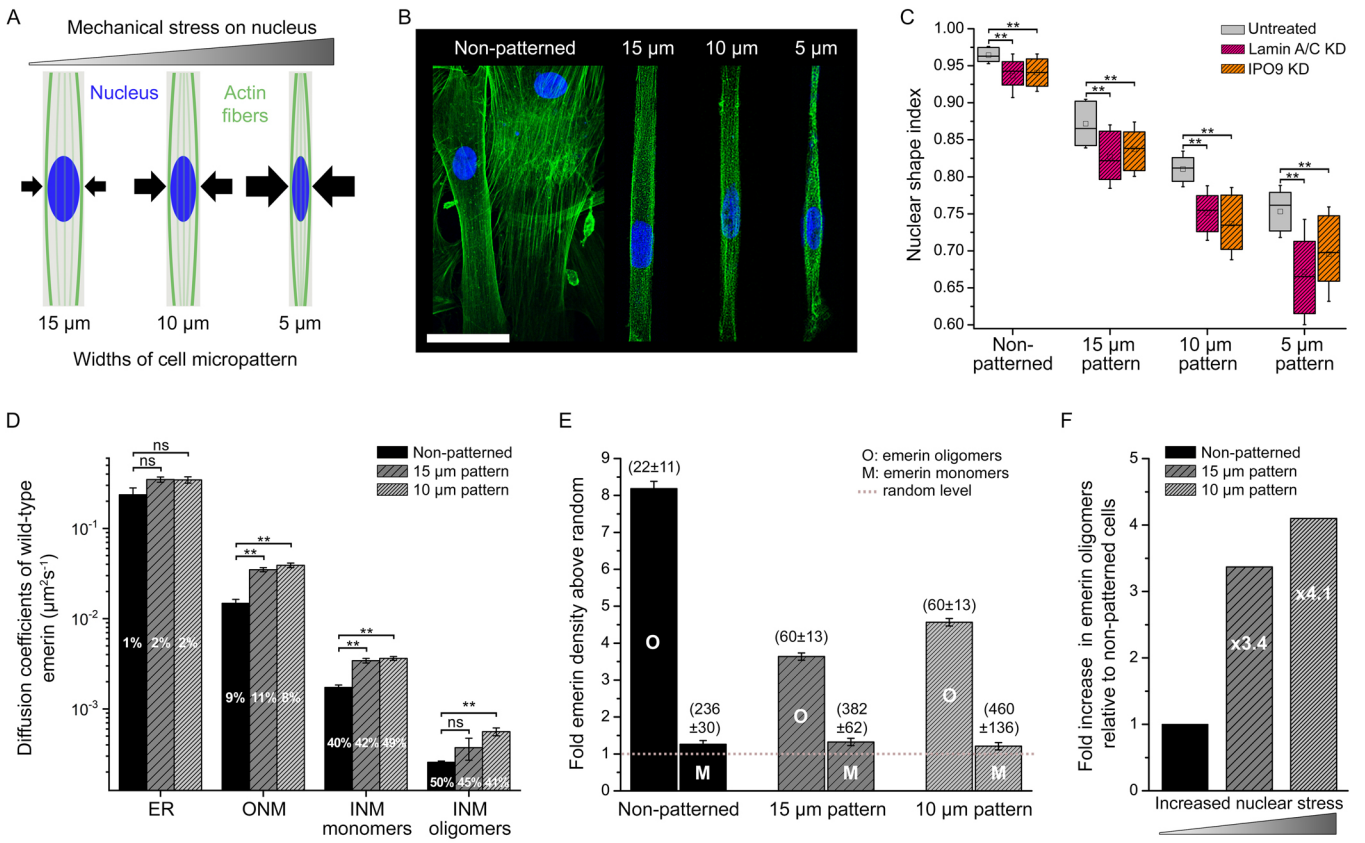

Fig. 4. Mechanical stress increases emerin mobility and the formation of emerin oligomers. (A) Schematic of increasing nuclear mechanical stress by cell micropatterning. Arrows represent force. (B) Confocal imaging of actin (green) and the nucleus (blue) in micropatterned *EMD*$^{+/y}$ HDFs. Images representative of two experiments for each micropattern width. Scale bar: 50 µm. (C) Nuclear shape index as a function of micropattern width in *EMD*$^{+/y}$ HDFs depleted for lamin A/C or nuclear actin. The box represents the 25–75th percentiles, and the median is indicated. The whiskers mark the s.d. of the mean, and the squares indicate the mean. Wilcoxon test, $^{**}P<0.01$. (D) Diffusion coefficients (mean±s.e.m.) and percentages of wild-type emerin in non-patterned cells or after nuclear deformation on 15 and 10 µm micropatterns. $^{**}P<0.01$; ns, not significant (two-tailed unpaired *t*-test). (E) Molecular densities above random (mean±s.e.m.) for wild-type emerin oligomers (O) and monomers (M) in non-patterned *EMD*$^{-/y}$ HDFs and after nuclear deformation on 15 and 10 µm micropatterns. Values in parentheses represent the size (mean±s.e.m.) of each domain in nanometers. (F) Increase in emerin oligomers as a function of nuclear stress. The numbers inside the histograms represent the fold increase from non-patterned cells. Sample sizes (*n*) in C–F are provided in the Materials and Methods.

PA-TagRFP–emerin was similar to that of wild-type emerin at the ER and the ONM (not significant, Fig. 6A; Table S1), but that both Q133H monomers and oligomers diffused significantly faster at the INM ($P<0.01$ and $P<0.05$, Fig. 6A). Previous *in vitro* studies have indicated that the Q133H mutation disrupts emerin binding to actin (Holaska et al., 2004) but does not impede interactions with lamin A/C (Holt et al., 2001), SUN1 (Haque et al., 2010) or BAF (Bengtsson and Wilson, 2004). The increased INM diffusion of Q133H therefore suggests that it does not bind nuclear actin. Interestingly, this faster INM diffusion of Q133H resembled the increased mobility of wild-type emerin when nuclear actin was depleted (Fig. 2A), which further indicates that nucleoskeletal actin modulates the diffusion of emerin monomers and oligomers. This is consistent with previous observations showing that emerin expression influences the mobility of nuclear actin (Ho et al., 2013) and is indicative of a reciprocal effect of emerin–nuclear actin interactions on their respective mobilities. The diffusion of Q133H at the INM was also similar to that of wild-type emerin under mechanical stress in both 15 µm- and 10 µm-wide micropatterns (not significant, Fig. S8), which supports a mechanism where nuclear deformations involve a dissociation of emerin from nuclear actin that leads to faster emerin diffusion at the INM.

Although, it was reported that Q133H has a reduced capacity to self-assemble *in vitro* (Herrada et al., 2015), its spatial distribution and cluster maps showed that it organized into monomers and oligomers across the INM (Fig. 6B,C). Like wild-type emerin, Q133H monomers were distributed in 213±62 nm (mean±s.e.m.) membrane domains (Fig. 6B), indicating that the inability to bind nuclear actin increases the mobility of Q133H monomers but does not affect their overall spatial distribution at the INM. Q133H also maintained the ability to self-assemble at the INM where it formed oligomeric clusters with sizes of 19±12 nm, which are comparable to the 22±11 nm size of wild-type emerin oligomers, but with molecular densities 12.2±0.2-fold above random (Fig. 6B,C; Table S2). This 50% increase in oligomerization compared to wild-type indicates that deficient binding of Q133H to nucleoskeletal actin leads to a disproportionate self-assembly of emerin into oligomeric nanodomains. It also implies that direct binding to nuclear actin normally reduces the oligomerization potential of wild-type emerin, consistent with our observation that excessive nuclear accumulation of actin impeded the formation of emerin oligomers at the INM (Fig. S7).

Δ95-99 mutation

When we performed similar studies with Δ95-99 emerin, we found that diffusions at the ER membrane and the ONM were unchanged compared to wild-type emerin (not significant, Fig. 6D; Table S1), but that lateral mobilities at the INM were significantly reduced ($P<0.05$

Journal of Cell Science (2022) 135, jcs258969. doi:10.1242/jcs.258969

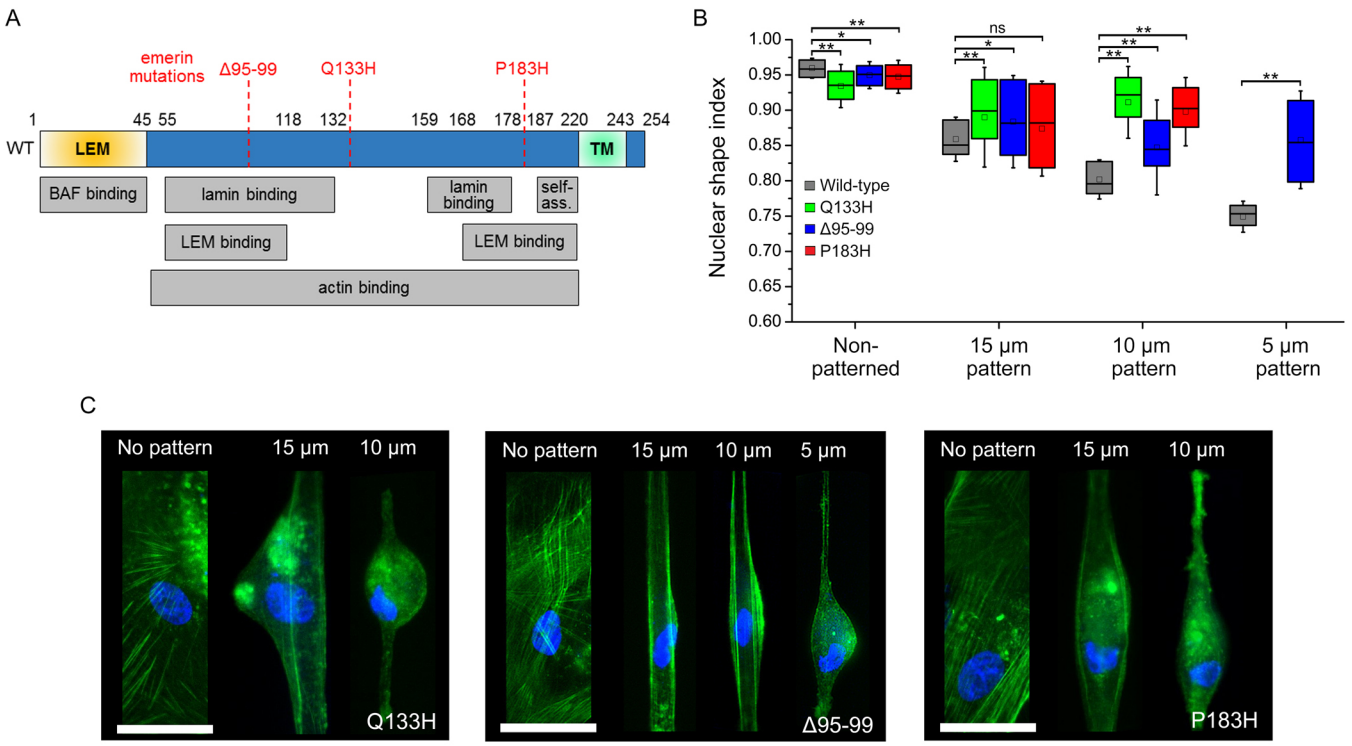

Fig. 5. Emerin mutations induce defective nuclear shape adaptation against mechanical stress. (A) Diagram of emerin with binding and self-association domains (self-ass.) and position of Δ95-99, Q133H and P183H mutations. (B) Nuclear shape index as a function of micropattern width for *EMD*$^{-/y}$ HDFs expressing wild-type, Q133H, Δ95-99 or P183H emerin. The box represents the 25–75th percentiles, and the median is indicated. The whiskers mark the s.d. of the mean, and the squares indicate the mean. Sample sizes (*n*) are provided in the Materials and Methods. **P*<0.05; ***P*<0.01; ns, not significant (Wilcoxon test). (C) Fluorescence imaging of actin (green) and the nucleus (blue) in micropatterned *EMD*$^{-/y}$ HDFs expressing Q133H, Δ95-99 or P183H emerin. Images representative of three experiments for each micropattern width. Scale bars: 50 µm.

and P<0.01, Fig. 6D), with the slowest Δ95-99 emerin population being essentially immobile. This suggests that Δ95-99 emerin interacts more strongly or more frequently than wild-type emerin with some of its binding partners on the nucleoplasmic side of the NE. Previous biochemical studies have shown that the Δ95-99 mutation disrupts emerin interactions with most of its binding partners, including lamin A/C and actin, but not BAF (Berk et al., 2013b). As BAF binding strongly influences the mobility of wild-type emerin (Fig. 2A), the reduced diffusion of Δ95-99 at the INM could stem from repetitive interactions with BAF, as recently proposed (Samson et al., 2017). To destabilize these interactions, we attempted to track Δ95-99 in *EMD*$^{-/y}$ HDFs knocked down for endogenous BAF and expressing BAF^{L58R}. Co-expression of both Δ95-99 and BAF^{L58R}, however, proved toxic to cells, indicating that the interactions between Δ95-99 emerin and BAF are important to maintain cell viability.

In addition to its slow mobility, Δ95-99 displayed defective oligomerization at the INM. Δ95-99 was distributed randomly over large, 420±51 nm NE domains and in smaller, 48±14 nm nanodomains where the molecular density of 1.3±0.1-fold above random was greatly reduced compared to wild-type emerin oligomers (Fig. 6E; Table S2). Effectively, Δ95-99 formed less dense and fewer oligomerization nanodomains in cluster maps (Fig. 6F). Thus, Δ95-99 does not efficiently oligomerize at the INM, consistent with its impaired self-assembly *in vitro* and that this deletion lowers emerin–emerin proximity (Herrada et al., 2015). Interestingly, despite an intact lamina and the preserved ability of Δ95-99 to bind SUN1 (Haque et al., 2010), the molecular densities and cluster maps of Δ95-99 were similar to those of wild-type emerin when the expression of lamin A/C was reduced or when SUN1 LINC complexes were disrupted (Fig. 3C,D). This reduced oligomerization of Δ95-99 emerin to oligomerization levels of wild-type emerin seen after lamin A/C depletion implies that direct binding to lamin A/C is required to stabilize emerin oligomers at SUN1 LINC complexes. This stabilizing role of lamin A/C is consistent with prior proximity ligation assays where Δ95-99 was found to be less close to lamin A/C than wild-type emerin (Herrada et al., 2015) and studies showing that the deletion abolishes direct lamin A/C binding to emerin (Lee et al., 2001). Together, these results show that Δ95-99 primarily distributes at random across the INM due to its reduced self-assembly, its inability to directly bind lamin A/C and its slow mobility.

P183H mutation

Like for the other emerin mutants, the diffusion of P183H emerin at the ER membrane and the ONM was unchanged compared to wild-type emerin (not significant, Fig. 6G; Table S1). However, its INM mobility was reduced for the populations attributed to monomers and oligomers (P<0.05 and P<0.01, Fig. 6G), with the slowest P183H population being immobile. This slow diffusion resembles that observed for Δ95-99 and again implies that, compared to wild-type emerin, P183H interacts more frequently with some of its nucleoplasmic binding partners. *In vitro*, P183H binds SUN1 (Haque et al., 2010), BAF and actin (Berk et al., 2013b), and also displays enhanced binding to lamin A/C compared to wild-type emerin (Lee et al., 2001). Its reduced INM mobility might therefore be linked to an increased binding frequency to BAF, like for Δ95-99, or to its enhanced binding to lamin A/C. The slow diffusion of P183H could also be due to the formation of dimers, which was suggested based on its strong propensity to self-assemble *in vitro*

Journal of Cell Science (2022) 135, jcs258969. doi:10.1242/jcs.258969

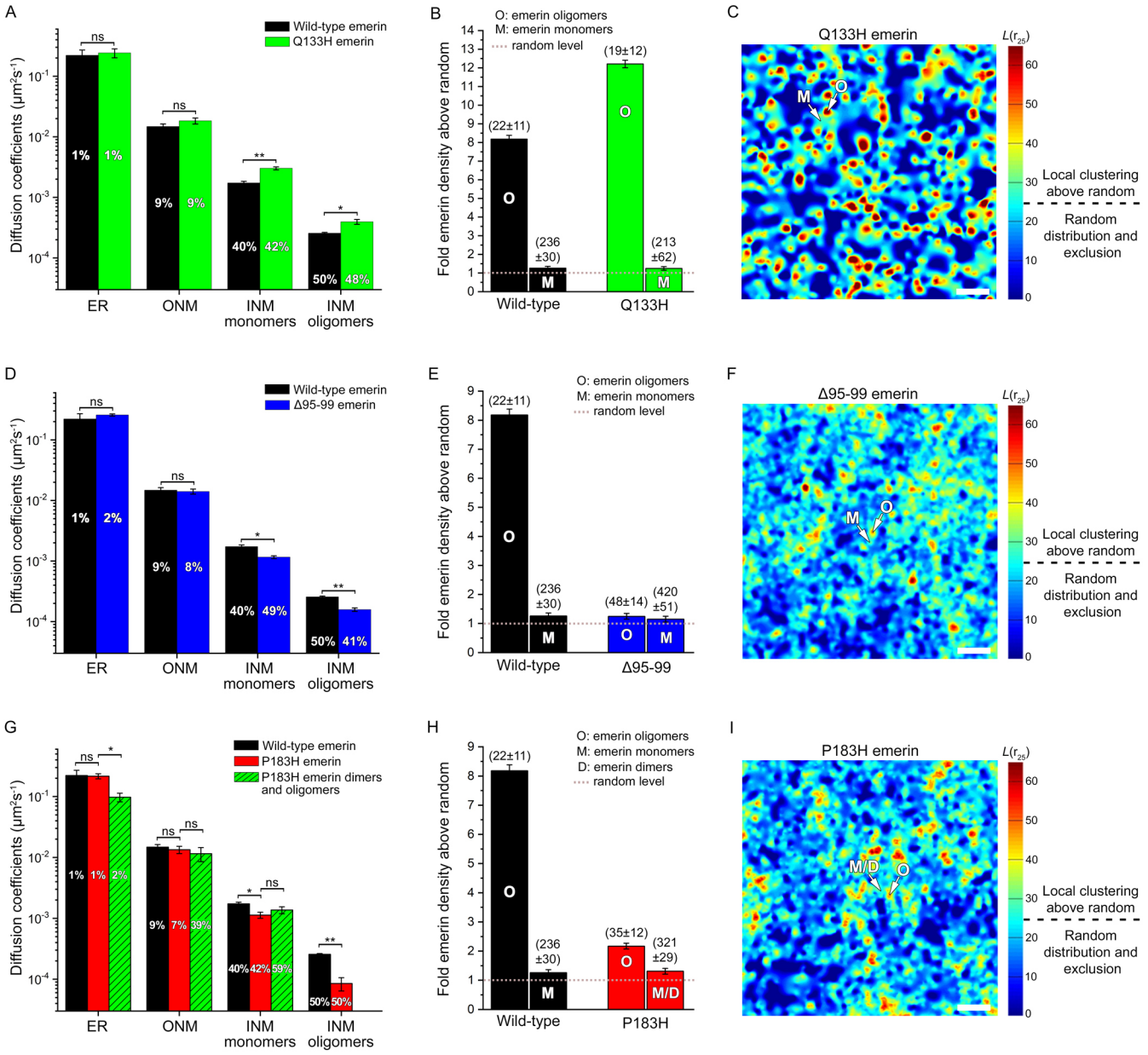

Fig. 6. Emerin mutants exhibit modified lateral mobilities and defective oligomerization. (A) Diffusion coefficients (mean±s.e.m.) and percentages of wild-type and Q133H emerin. (B) Molecular densities above random (mean±s.e.m.) for wild-type and Q133H emerin oligomers (O) and monomers (M). (C) Local cluster map of Q133H emerin. M, monomer areas; O, oligomer nanodomains. Scale bar: 250 nm. (D) Diffusion coefficients (mean±s.e.m.) and percentages of wild-type and Δ95-99 emerin. (E) Molecular densities above random (mean±s.e.m.) for Δ95-99 (208,092 localizations, 8 nuclei) and wild-type emerin oligomers (O) and monomers (M). (F) Local cluster map of Δ95-99 emerin. Scale bar: 250 nm. (G) Diffusion coefficients (mean±s.e.m.) and percentages of wild-type and P183H emerin compared to complemented P183H emerin–GFP–emerin species. (H) Molecular densities above random (mean±s.e.m.) for P183H and wild-type emerin oligomers (O) and monomers and dimers (M/D). (I) Local cluster map of P183H emerin. M/D, monomer and dimer areas; O, oligomer nanodomains. Scale bar: 250 nm. *P<0.05; **P<0.01; ns, not significant (two-tailed unpaired t-test). For B, E and H: values in parentheses represent the size (mean±s.e.m.) of each domain in nanometers. Images in C, F and I are representative of 6, 8 and 6 cell nuclei, respectively. Sample sizes (n) in A,B,D,E,G,H are provided in the Materials and Methods.

(Herrada et al., 2015) and observations that residue P183 is positioned in the 168-186 aa region required to limit emerin–emerin association (Berk et al., 2014). To determine whether P183H forms dimers, we performed tracking by CALM after co-expression of P183H fused to split-GFP fragments. Three populations of P183H–GFP–P183H emerin species were detected: a 2% population with a mobility slightly slower than P183H at the ER membrane (P<0.05, Fig. 6G), a larger 39% population with a mobility comparable to the ONM behavior of P183H (not significant, Fig. 6G), and a dominant 59% population with a lateral diffusion similar to the INM population initially attributed to P183H monomers by sptPALM (not significant, Fig. 6G; Table S1). Surprisingly, fluorescent species with diffusion coefficients matching that of the immobile P183H oligomers were not detected (Fig. 6G). The frequent detection of complemented P183H–GFP–P183H emerin species at both the ER membrane and the ONM indicates that P183H is indeed more prone to form dimers than wild-type emerin before reaching the INM. This seemingly biased monomer to dimer equilibrium towards dimers is maintained at the INM where it precludes an efficient association of

Journal of Cell Science (2022) 135, jcs258969. doi:10.1242/jcs.258969

P183H into oligomer domains, particularly if dimers are stabilized by irreversible assembly of the split-GFP fragments. This indicates that P183H has a strong propensity to form dimers that could impact oligomerization at the INM.

Consistent with these observations, the dimerization of P183H led to a significantly reduced oligomerization at the INM. P183H monomers and dimers were distributed in domains with typical sizes of 321±29 nm and molecular densities of 1.3±0.1-fold above random (Fig. 6H; Table S2). Smaller, 35±12 nm nanodomains were also observed, but their molecular density was reduced to 2.2±0.1 compared to wild-type oligomers (Fig. 6H). Indeed, although P183H could still bind lamin A/C and SUN1, it forms oligomeric domains, having lower molecular density than wild-type emerin in cluster maps (Fig. 6I), indicating that the dimerization of P183H hinders further self-association into dense oligomers at the INM.

Abnormal reorganization of Δ95-99 emerin in response to mechanical stress

To characterize the importance of emerin oligomerization for nuclear deformation and responses to mechanical stress, we also studied the nanoscale reorganization of Δ95-99 in micropatterned cells. For deformed nuclei in 15 µm patterns, Δ95-99 monomers were dispersed over large 810±215 nm (mean±s.e.m.) INM domains, almost double the size of monomer domains in non-stressed nuclei (Fig. 7A). However, as stress became more pronounced in 10 µm patterns, the dispersion of Δ95-99 monomers receded, with distributions in the 499±250 nm domains (Fig. 7A). Thus, in contrast to wild-type emerin, a progressive dispersion of Δ95-99 monomers over increasingly large INM areas was not observed with increasing mechanical stress, consistent with the abnormal changes in NSI induced by the deletion. The formation of emerin oligomers remained limited, with Δ95-99 molecular densities increasing slightly from 1.3±0.1-fold to 1.7±0.1- and 2.0±0.1-fold above random in 15 µm and 10 µm micropatterns, respectively (Fig. 7A; Table S2). With the concurrent enlargement of nanodomains from 48±14 nm to 81±16 nm and 75±20 nm, the relative oligomerization of Δ95-99 compared to non-mechanically stressed nuclei increased by 3.9-fold initially, but did not rise further as nuclear stress intensified (Fig. 7B). Δ95-99 oligomeric nanodomains remained sparser and less dense than for wild-type emerin in cluster maps of nuclei under stress (Fig. 7C). Thus, the failure of Δ95-99 to gradually self-associate at sufficiently high molecular densities leads to defective nuclear responses to mechanical forces. These data underline the importance of modulating the oligomerization of emerin as a function of mechanical stress intensity for adaptive nuclear deformations.

DISCUSSION

Combining single-molecule imaging and quantitative measurements, we showed that emerin distributes as monomers and oligomers at the INM and that clinically relevant EDMD mutations induce modified emerin mobility and nanoscale organizations. The oligomerization of emerin is modulated by its ability to engage or disengage interactions with various structural elements juxtaposed to the INM, including lamin A/C, SUN1, nuclear actin and BAF. Regulated expressions of lamin A/C and SUN1, together with functional LINC complexes, are essential for the formation and the stabilization of emerin oligomers, whereas balanced interactions of emerin with BAF and nuclear actin further modulate its diffusion and its oligomerization potential. We also showed that the mechanotransduction functions of emerin are coupled to its oligomeric state, with the formation and maintenance of emerin oligomers being central to nuclear shape adaptation against mechanical forces. Indeed, EDMD-inducing mutations that affect the self-assembly of emerin and its binding to structural elements at the INM lead to abnormal nuclear deformations and defective nuclear positioning in response to mechanical stress.

Although the altered *in vitro* binding properties of Q133H, Δ95-99 and P183H emerin mutants resulted in expected differences in organization in cells, they did not necessarily induce fully predictable changes in diffusion and distribution at the NE. In effect, via its flexible IDR, emerin appears to mediate complex interactions with itself, lamin A/C, SUN1, nuclear actin and BAF, where binding to one partner impacts oligomerization and, interdependently, affects interactions with other partners. Our study on the organization of wild-type emerin after nuclear actin depletion or accumulation, and of the Q133H emerin mutant, which is known to have disrupted binding to actin, reveals that binding to nuclear actin significantly influences the mobility and the oligomerization potential of emerin. Actin binding to the IDR of emerin could mask interaction domains that normally serve as LEM binding and self-association sites between emerin monomers (Berk et al., 2014). IDR masking, combined with the reduced lateral mobility of actin-bound emerin, might therefore modulate the formation of oligomers by limiting molecular collisions between emerin monomers. Consistent with the need to precisely adjust the oligomerization potential of emerin for adaptive nuclear shape deformations, increased emerin diffusion and controlled formation of emerin oligomers are coupled molecular events during nuclear adaptation against stress, as shown by our measurements in micropatterns. We thus speculate that the deficient binding of Q133H emerin to nuclear actin and its higher oligomerization at SUN1 LINC complexes are linked to the abnormal nuclear deformations observed in cells.

The differential interactions of emerin with its nucleoplasmic partners and their influence on its mobility and its oligomerization are also underlined by the surprisingly slow mobility of Δ95-99 emerin, which does not bind lamin A/C nor actin *in vitro*, but binds BAF. The 48-118 aa region of emerin, where the Δ95-99 mutation occurs, has been suggested to act as a binding site for the LEM domain (Berk et al., 2014) and, through altered region flexibility, it is possible that the deletion reduces the efficacy of such interactions, potentially causing the LEM domain to bind BAF more frequently (Samson et al., 2017). Repeated interaction of Δ95-99 emerin with BAF and, indirectly, with the lamina or chromatin via ternary BAF complexes could slow its diffusion, limit molecular collisions, and impede its oligomerization by sequestering the LEM domain and reducing bridging interactions with LEM binding sites on other emerin molecules. The Δ95-99 deletion, which occurs within the 55-132 aa lamin tail-binding region of emerin (Berk et al., 2014), could also prevent a stabilization of already sparse Δ95-99 oligomers by direct lamin A/C binding. We thus postulate that the aberrant nuclear deformations against mechanical stress in cells expressing Δ95-99 emerin stem from unbalanced interactions of this mutant with BAF and its inability to form lamin A/C-stabilized oligomers at SUN1 LINC complexes.

A similar impairment of *in trans* interactions between the LEM domain and self-association sites along the joined IDR of P183H dimers likely results in their reduced ability to oligomerize, despite retained binding to lamin A/C and SUN1. The reported enhanced binding of lamin A/C to P183H emerin (Lee et al., 2001) that occurs in close proximity to these same self-association sites could also interfere with inter-emerin bridging interactions. In both cases, the inability of the LEM domain to access binding sites along the IDR

Journal of Cell Science (2022) 135, jcs258969. doi:10.1242/jcs.258969

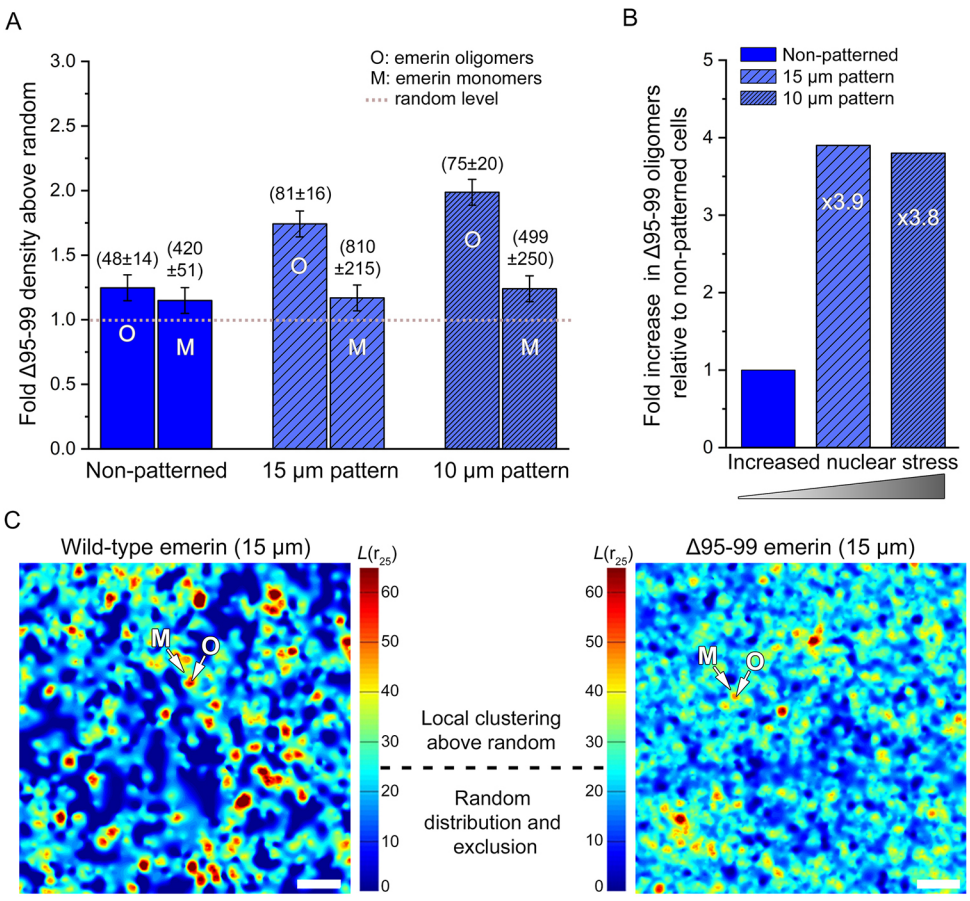

Fig. 7. Insufficient oligomerization of Δ95-99 emerin mutant against mechanical stress. (A) Molecular densities above random (mean±s.e.m.) for Δ95-99 emerin oligomers (O) and monomers (M) in non-patterned cells or after nuclear deformation on 15 and 10 µm micropatterns. Values in parentheses represent the size (mean±s.e.m.) of each domain in nanometers. Sample sizes (*n*) are provided in the Materials and Methods. (B) Changes in Δ95-99 emerin oligomers as a function of nuclear stress on 15 and 10 µm micropatterns. The numbers inside the histograms represent the fold increase from non-patterned cells. (C) Local cluster maps of wild-type and Δ95-99 emerin after nuclear deformation on 15 µm micropatterns. M, monomer areas; O, oligomer nanodomains. Images representative of 10 and 5 cell nuclei, respectively. Scale bar: 250 nm.

would elicit its repeated interactions with BAF, leading to the observed slow diffusion of P183H at the INM. The defective nuclear shape adaptation to mechanical challenges of cells expressing P183H might thus arise from emerin dimerization and excessive interactions with BAF or lamin A/C that prevent the efficient formation of emerin oligomers at LINC complexes. Our observation that lamin A/C overexpression, which was previously shown to induce the nuclear accumulation of BAF (Loi et al., 2016), leads to the decreased oligomerization of wild-type emerin is indeed consistent with the need to modulate emerin–BAF–lamin A/C tripartite interactions to promote the self-assembly of emerin.

We have shown that Δ95-99 emerin does not self-assemble into sufficiently dense oligomers at the INM, and thus it induces aberrant nuclear shape remodeling against mechanical stress. The phosphorylation of emerin residues Y74 and Y95 was previously shown to mediate the recruitment of lamin A/C to the LINC complex during nuclear stiffening in response to mechanical force (Guilluy et al., 2014). Our observation that Δ95-99 fails to promote adaptive nuclear deformation in response to mechanical cues due to its reduced ability to form lamin A/C- and SUN1-stabilized oligomers is consistent with the major role played by Y95 phosphorylation for emerin-mediated mechanotransduction at the NE. The abnormal organization of cytoskeletal actin in mechanically challenged cells expressing Δ95-99 emerin, akin to disorganizations detected with a non-phosphorylatable double tyrosine mutant (74-95FF) of emerin (Guilluy et al., 2014), also suggests that emerin oligomers strengthen the connection between lamin A/C, the LINC complex and cytoskeletal filaments to promote correct nuclear positioning and deformation. These data point towards a link between Y95 phosphorylation, emerin oligomerization and recruitment of lamin A/C for stiffening the NE at LINC complexes, likely driven by phosphorylation-induced changes in emerin conformation (Berk et al., 2013a; Tifft et al., 2009). It is thus possible that emerin oligomeric nanodomains are enriched in Y95 phosphorylated emerin, lamin A/C and LINC complex components, whereas emerin monomers populate the rest of the INM, consistent with emerin enrichment in distinct nucleoskeletal ‘niches’ at the NE (Berk et al., 2013a).

Taken together, these findings support a model in which, during the stress response, emerin monomers transiently unbind from nuclear actin and BAF, such that their increased lateral diffusion at the INM and exposure of both the LEM domain and self-association sites along their IDR favor their oligomerization at LINC complexes (Fig. 8). Within emerin oligomers, stabilization by direct interactions with lamin A/C and SUN1 and further modulation of emerin self-association by nuclear actin and BAF likely allow for a precise regulation of the size of emerin oligomeric nanodomains, as needed for adaptive nuclear deformation in response to forces transmitted at LINC complexes. Indeed, as we have shown, emerin oligomers have a localized distribution at the INM, are stabilized by lamin A/C and SUN1, are disrupted following interference with the organization of LINC complexes and their formation relies on a part of the emerin IDR that requires phosphorylation for the recruitment of lamin A/C to LINC complexes (Guilluy et al., 2014). These observations are consistent with the idea that emerin oligomers are sites where interactions between emerin, lamin A/C and LINC components are strengthened. It was recently suggested that the clustering of SUN proteins could enable them to sustain high mechanical loads at the NE during force-dependent processes (Jahed et al., 2018). We propose that emerin oligomerization at SUN1 LINC complexes

Journal of Cell Science (2022) 135, jcs258969. doi:10.1242/jcs.258969

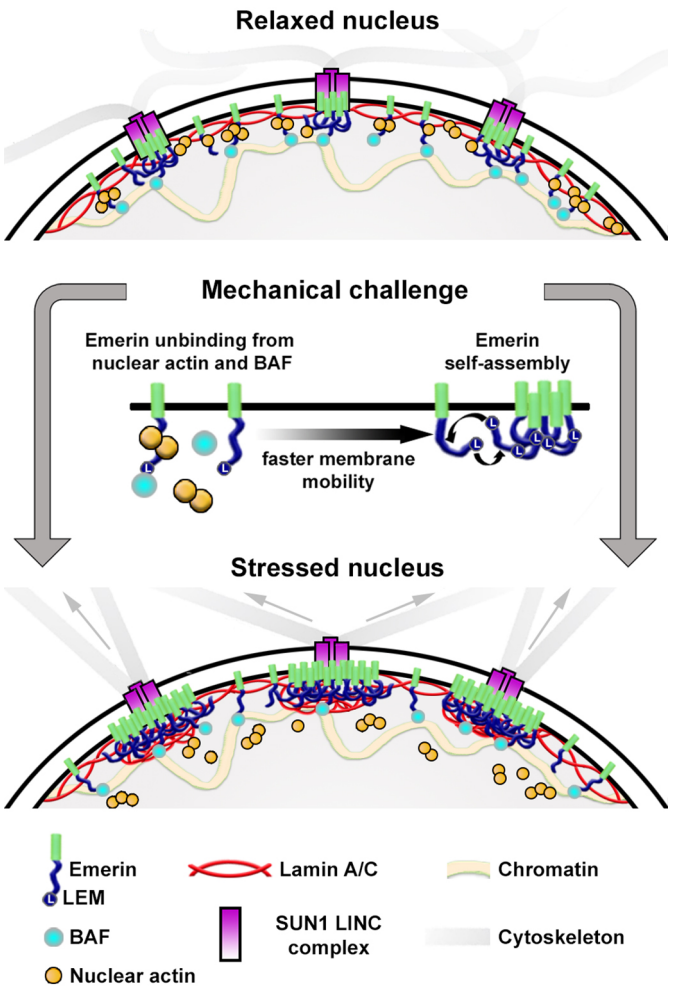

Fig. 8. Model of emerin re-organization at the nuclear envelope in response to mechanical challenges. Emerin monomer unbinding from nuclear actin and BAF induces increased lateral mobility at the inner nuclear membrane and favors LEM domain interactions with binding sites along the intrinsically disordered region of other emerin, for the controlled formation of emerin oligomers at SUN1 LINC complexes and their stabilization by lamin A/C.

might therefore contribute to the increased connectivity between the nucleoskeleton, the NE and the cytoskeleton for anchoring the nucleus and providing force absorption contact points during nuclear deformation.

In response to surging mechanical stress, the incremental oligomerization of emerin in enlarged nanodomains that we observed could be part of a mechanism that redistributes increasing forces over wider areas at LINC complexes to maintain a basal membrane pressure at these anchoring points between the nucleoskeleton, the NE and the cytoskeleton. Beyond this central role played by emerin self-assemblies, emerin might have additional functions outside these anchoring oligomeric nanodomains. For instance, the disengagement of emerin monomers from nuclear actin likely reduces NE contacts with the nucleoskeleton, whereas some membrane connectivity with nuclear chromatin is maintained via BAF. Indeed, both the nucleoskeleton and chromatin tethering to the NE participate in nuclear mechanics (Stephens et al., 2017). Together, strengthening the connections between the NE, the lamina and the cytoskeleton at LINC complexes, but partially relaxing them in the rest of the membrane could provide means to couple the controlled nuclear deformation with nucleus positioning in cells. As we showed, such coupling is defective with emerin mutants.

Additional cross-correlative studies will be needed to further define how the structural interdependencies between emerin monomers, emerin oligomers, SUN1, BAF, and key nucleoskeletal elements spatially regulate INM–lamina and INM–chromatin contacts and reinforce the connections between the NE and the cytoskeleton at LINC complexes during nuclear responses to mechanical force. At the center of these processes, emerin diffusion and monomer-oligomer exchange facilitate the transduction of mechanical cues throughout the entire NE, for coordinated changes in local nuclear stiffness and remodeling of the nuclear shape.

MATERIALS AND METHODS

Cell culture, emerin expression and cell staining

Emerin-null human dermal fibroblasts ($EMD^{-/y}$ HDFs) and normal dermal fibroblasts ($EMD^{+/y}$ HDFs) were kindly provided by Dr Howard Worman, Columbia University, USA, and regularly tested for contaminations. $EMD^{-/y}$ HDFs are derived from a male EDMD patient (G-9054) and carry a 59-nucleotide deletion within the *EMD* gene (*EMD* g.329del59) that ablates emerin expression (Talkop et al., 2002). HDFs were grown in Dulbecco's Modified Eagle Medium (DMEM, Lonza) with 10% fetal bovine serum (FBS, Gibco-Life Technologies), 50 units ml^{-1} penicillin and 50 µg ml^{-1} streptomycin (complete medium) and maintained at 37°C in a humidified atmosphere with 5% CO_2.

Human wild-type emerin cDNA was kindly provided by Dr Juliet Ellis, University College London, UK. For the expression of PA-TagRFP–emerin, a pEGFP-N1 plasmid (Clontech) backbone encoding emerin fused to the C-terminus of PA-TagRFP was produced by XbaI and KpnI insertion and PCR fusion of the human emerin cDNA. Cells plated on fibronectin-coated glass coverslips were transfected with PA-TagRFP–emerin using X-tremeGENE HP (Roche). At 48-72 h post transfection, live cells were imaged by sptPALM in Hank's Balanced Salt Solution (HBSS) buffer at 37°C. For micropatterning experiments, cells grown on six-well plates were trypsinized after 48-72 h of transfection and plated on fibronectin-micropatterned coverslips.

To express SNAP–emerin, human emerin was first fused to the C-terminus of a SNAP-tag by AscI and XhoI insertion in a pSNAP-tag(m) plasmid (NEB). SNAP–emerin was then subcloned into a modified pFUGW lentiviral vector (modified from Addgene #14883) by NheI and AgeI insertion. Lentiviral particles for the expression SNAP–emerin were produced by the UCLA Vector Core. Transduction of HDFs grown at 70% confluence on six-well plates was performed for 48 h, using 25 ng ml^{-1} of lentiviral particles in complete growth medium containing 8 µg ml^{-1} of polybrene, after which the medium was replaced. Following another 24 h incubation, cells were trypsinized, and plated on fibronectin-coated or fibronectin-micropatterned coverslips. For imaging, cells were fixed with 4% paraformaldehyde in PBS for 15 min, permeabilized with 0.1% Triton X-100 (Sigma-Aldrich) for 15 min and blocked with 4% bovine serum albumin (BSA, Sigma-Aldrich) and 0.1% Tween 20 (Sigma-Aldrich) for 30 min at room temperature. Cells were then stained with 1 µM of SNAP-Surface-Alexa Fluor 647 (BG-A647, NEB) in 4% BSA and 0.1% Tween 20 for 1 h at 37°C, then thoroughly washed before super-resolution imaging.

For the expression of split-GFP–emerin, humanized cDNA for split-GFP 1-10 (Pinaud and Dahan, 2011) was inserted by NheI and XbaI digestion in the pEGFP-N1 plasmid backbone encoding emerin and expressed as an N-terminal fusion to emerin. The shorter 11th β-sheet M3 fragment (Pinaud and Dahan, 2011) was also fused to the N-terminus of emerin by PCR cloning using primers (sequences available upon request) encoding the M3 fragment sequence and subcloning into the pEGFP-N1 backbone via NheI and XhoI digestions. Both plasmids were co-transfected in HDFs using X-tremeGENE HP (Roche) as described for PA-TagRFP–emerin, and cells were imaged by CALM 48-72 h post-transfection. All constructs were verified by sequencing.

For immunostaining of emerin, cells were grown on coverslips, fixed and permeabilized as described for SNAP–emerin staining. Cells were labeled

Journal of Cell Science (2022) 135, jcs258969. doi:10.1242/jcs.258969

with a rabbit anti-emerin antibody (1:500, Santa Cruz Biotechnology, sc-15378) for 45 min, washed in PBS and further labeled with a goat anti-rabbit-IgG antibody conjugated to Alexa Fluor 488 (1:400, Invitrogen) for 45 min. After washing, cells were mounted in a DAPI-Fluoromount G (Electron Microscopy Sciences) and imaged by confocal microscopy.

To label cytoplasmic actin and measure nuclear shape indices, cells were fixed with 4% paraformaldehyde in PBS for 15 min, permeabilized with 0.1% Triton X-100 for 10 min, and blocked with 4% BSA and 0.1% Tween 20 for 1 h. Cells were stained with phalloidin-iFluor 488 (1:1000, cat. no. ab176753, Abcam) for 1 h, washed with PBS, mounted in DAPI-Fluoromount G and imaged by confocal or wide-field microscopy.

Mutations, siRNA and exogenous protein expressions

Emerin mutations Q133H and P183H were introduced in PA-TagRFP–emerin, SNAP–emerin and emerin fused to both split-GFP fragments by site-directed mutagenesis using QuickChange Lightning Site Directed Mutagenesis (Agilent) and mutagenic primer pairs [Q133H, 5′-CGCTTTCCATCACCATGTGCATGATGA-3′ and 5′-GATCGTCATC-ATGCACATGGTGATGGA-3′; P183H, 5′-CCTGTCCTATTATCATACT-TCCTCCTC-3′ and 5′-GTGGAGGAGGAAGTATGATAATAGGA-3′].

The Δ95-99 emerin deletion was produced using partially phosphorothioated PCR primers and T7 exonuclease digestion, as previously described (Stoynova et al., 2004). Primer pairs for the Δ95-99 deletion were 5′-GACTACTTCACCA*C*C*C*A*GGACTTAT-3′ and 5′-GGTGAAGTAGTCG*T*C*A*TTGTAGCC-3′, where * denotes phosphorothioate modifications. All primers were obtained from Integrated DNA Technologies (IDT) and all mutations were verified by sequencing.

siRNA duplex for BAF, SUN1 and Dicer siRNA for lamin A/C, SUN1 and controls were obtained from IDT. The sequences of sense nucleotides were as follows: BAF siRNA, 5′-AGAUUGCUAUUGUCGUACUUU-3′; lamin A/C DsiRNA #1, 5′-AGCUGAAAGCGCGCAAUACCAAGaa-3′; Lamin A/C DsiRNA #2, 5′-GGAACUGGACUUCCAGAAGAACAtc-3′; SUN1 DsiRNA #1, 5′-GCUUUUAGUAUCAACCACGUGUCaa-3′; SUN1 siRNA #2, 5′-CCAUCCUGAGUAUACCUGUCUGUAU-3′; and control DsiRNA, 5′-CGUUAAUCGCGUAUAAUACGCGUat-3′ (IDT#51-01-14-04).

siRNA duplex for IPO9 was obtained from Ambion (ID: S31299) and siRNA for the nuclear actin exporter XPO6 was obtained from Qiagen (ID: SI00764099). All siRNA were transfected or co-transfected with emerin plasmids at 25 nM using X-tremeGENE HP (Roche). When associated with lentiviral expression of emerin, siRNA transfection was performed 2 h before viral titer application.

Exogenous BAF^{L58R} was expressed from an EGFP-BAF^{L58R} lentiviral plasmid (Samwer et al., 2017) and lentiviral particles were produced by the UCLA Vector Core. HDF cells were transduced with 25 ng ml^{-1} of lentiviral particles as described for SNAP–emerin. For rescue of lamin A/C expression and overexpression experiments, cDNA encoding for an exogenous siRNA-resistant human lamin A/C (Frock et al., 2006) was kindly provided by Dr Richard Frock, Stanford University, USA and used together with lamin A/C DsiRNA #2, designed to knockdown endogenous lamin A/C. For rescue of SUN1 expression and overexpression experiments, cDNA encoding for an exogenous siRNA-resistant human SUN1 fusion to EGFP (EGFP-SUN1) was kindly provided by Dr Christine Doucet, Centre de Biochimie Structurale, Montpellier, France and used together SUN1 siRNA #2, designed to knockdown endogenous SUN1, as previously described (Talamas and Hetzer, 2011). Exogenous expression of mCherry-DN-KASH was achieved by cell transfection of the mammalian expression plasmid #125553, obtained from Addgene.

Cell micropatterning and nuclear shape index measurements

HDFs were micropatterned as described previously (Bautista et al., 2019; Fernandez et al., 2017). Briefly, hexamethyldisilazane-activated glass coverslips (Marienfeld, #1.5, Ø25 mm) were stamped with rectangular and fibronectin-coated polydimethylsiloxane stamps having lengths of 210 µm and widths of 15 µm, 10 µm or 5 µm, respectively. Cell attachment outside the fibronectin strips was blocked with a 1% solution of Pluronic F-127. After attachment for 1 h and removal of unattached cells, HDFs were allowed to spread out on the micropatterns for 6 h at 37°C before being prepared for microscopy imaging.

Using ImageJ (Schneider et al., 2012), the nuclear shape index (NSI) was determined by measuring the nuclear cross-sectional area and the nuclear perimeter of DAPI-stained nuclei imaged by wide-field microscopy, and by calculating the ratio:

$$\mathrm{NSI} = \frac{4 \times \pi \times \mathrm{area}}{\mathrm{perimeter}^2}. \quad (1)$$

The NSI measures the roundness of the nucleus, with an NSI of 1 corresponding to a circular nuclear shape. Mean±s.d. NSI values were reported for multiple cell nuclei per condition. In graphs, the box length indicates the NSI interquartile range, the central square indicates the NSI mean, the central bar indicates the NSI median and the error bars indicate the standard deviation. The number of measured nuclei was n=54, 70, 61 and 62 nuclei for $EMD^{+/y}$ cells in non-patterned, 15, 10 and 5 µm wide patterns, respectively; n=75, 60, 70 and 66 nuclei for lamin A/C-depleted cells; and n=62, 71, 66 and 46 nuclei for nuclear actin-depleted cells. For $EMD^{-/y}$ cells expressing wild-type emerin, the number of measured nuclei was n=38, 33, 26 and 57 nuclei in non-patterned, 15, 10 and 5 µm wide patterns, respectively; n=74, 58 and 37 nuclei for Q133H emerin; n=64, 89, 45 and 46 nuclei for Δ95-99 emerin and n=82, 78 and 28 nuclei for P183H emerin. Significant differences between NSI values were evaluated using a Wilcoxon rank-sum test.

Microscopy imaging

Confocal imaging of immunostained emerin in normal HDFs, emerin-null HDFs and emerin-null HDFs after expression of wild-type PA-TagRFP–emerin was performed on an Olympus Fluoview FV1000 confocal microscope equipped with a 60×/1.40 NA objective, 405 nm and 488 nm lasers and appropriate emission filters for imaging DAPI (450/20 nm) and Alexa Fluor 488-labeled antibodies against emerin (510/10 nm).

Confocal imaging of nuclear deformation and actin organization in micropatterned $EMD^{+/y}$ HDFs was performed on a Zeiss LSM 700 microscope equipped with a C-Apochromat 63×/1.15 NA W Korr objective, excitation lasers at 405 nm and 488 nm and appropriate beamsplitter and emission channel settings for dual detection of DAPI and phalloidin-iFluor 488.

Wide-field imaging of labeled actin and labeled nuclei for NSI measurements was performed on an inverted Nikon Eclipse Ti-E microscope equipped with a 40× objective (Nikon), an iXon Ultra EMCCD camera (Andor), 405 nm and 488 nm lasers, a T495lpxr dichroic mirror and a 525/50 emission filter (Chroma) for phalloidin-iFluor 488 or a 458Di02 dichroic mirror and a 483/32 emission filter (Semrock) for DAPI.

SptPALM, dSTORM and CALM imaging were performed on an inverted Nikon Eclipse Ti-E microscope equipped with a 100×/1.49 NA objective (Nikon), an iXon EMCCD camera (Andor), perfect focus drift compensation optics, an astigmatic lens for 3D super-resolution imaging, a piezo z-scanner for calibration of 3D super-resolution images (Mad City Labs), laser lines at 405, 488, 561 and 647 nm (Agilent), a multiband pass ZET405/488/561/647x excitation filter (Chroma), a quad-band ZT405/488/561/647 dichroic mirror (Chroma) and appropriate emission filters for sptPALM imaging of PA-TagRFP (600/50 nm, Chroma), 3D-dSTORM imaging of Alexa Fluor 647 (700/75 nm, Chroma) and CALM imaging of complemented split-GFP (525/50 nm, Semrock).

sptPALM of PA-TagRFP–emerin was performed in 37°C HBSS buffer (Corning) by highly inclined and laminated optical sheet (HILO) excitation of the bottom nuclear membrane of cells with a continuous and low power photoactivation at 405 nm and an excitation at 561 nm. The HILO illumination angle was θ=51.6°. Images were acquired continuously at a frame rate of 40 ms per frame for no longer than 3 min per cell to limit UV damage. CALM imaging of complemented emerin–GFP–emerin species was performed as described for sptPALM but with a single HILO excitation at 488 nm.

dSTORM of SNAP–emerin labeled with BG-A647 was performed at room temperature in a photoswitching buffer composed of 10% glucose, 0.5 mg ml^{-1} glucose oxidase (Sigma), 40 µg ml^{-1} catalase (Sigma), and 1%

β-mercaptoethanol (Sigma). Continuous photoswitching was achieved with a low power 488 nm laser and imaging was performed with a 647 nm laser excitation at a frame rate of 80 ms per frame. *Z*-calibration and sample drift corrections were performed using a few 40 nm TransFluoSphere beads (488/685 nm, Life Technologies) as fiducial markers spread on the cell samples.

For rescue and overexpression experiments, dSTORM imaging of SNAP–emerin was performed only in cells expressing exogenous human lamin A/C, human EGFP-SUN1 or mCherry-DN-KASH, as identified by lamin A/C immunostaining, EGFP or mCherry fluorescence. In the case of lamin A/C and EGFP-SUN1 rescues, imaging was done in cells having relatively low exogenous expressions.

FRAP of emerin

FRAP of wild-type emerin and emerin mutants was done in U2OS cells transiently transfected with PA-TagRFP–emerin. Cells were imaged at 37°C in HBSS buffer (Corning) on an Olympus Fluoview FV1000 confocal microscope equipped with a 60×/1.40 NA oil immersion objective. PA-TagRFP–emerin at the bottom NE was briefly photoactivated by laser scanning at 405 nm and PA-TagRFP fluorescence was monitored every 2.8 s with a 543 nm laser. Circular regions of interest (7 µm in diameter) were photobleached and recorded. After background subtraction, FRAP curves were doubly normalized as previously described (Phair et al., 2004) to correct for loss of fluorescence due to bleaching during acquisition. FRAP curves from measurements on 9-12 cells per condition were averaged after normalization to full scale. After comparison of one- or two-component lateral diffusion models (Soumpasis, 1983), the apparent diffusion coefficients of emerin were determined by fitting FRAP curves with a two-component model using equations for a uniform circular bleach region (Soumpasis, 1983). A fast (D_{fast}=4.48×10^{-2}±1.0×10^{-2} µm^2/s, 17%) and slow (D_{slow}=4.0×10^{-3}±4×10^{-4} µm^2/s, 83%) diffusive behavior of wild-type emerin was observed by FRAP (Fig. S1), consistent with previous diffusion values (1.0×10^{-1}±1×10^{-2} µm^2/s and 7.50×10^{-2}±2.9×10^{-3} µm^2/s) (Haraguchi et al., 2008; Ostlund et al., 1999, 2006) and the reported presence of a nearly immobile emerin fraction at the NE (Haraguchi et al., 2008; Shimi et al., 2004). Emerin mutations P183H, Q133H and Δ95-99 did not display statistically significant differences in ensemble diffusion dynamics compared to wild-type emerin (Fig. S1).

Cell extracts and immunoblotting

After siRNA treatment, cells were harvested and fractionated as described previously (Berk et al., 2013a). Cells were scraped, centrifuged for 5 min at 4000 ***g*** and washed three times with PBS. Cell pellets were then flash frozen and stored at −80°C. Cells were thawed for 10 min on ice, and then for 10 min in 300 µl ice cold hypotonic lysis buffer [20 mM HEPES pH 7.4, 50 mM N-acetylglucosamine, 1 mM DTT, 100 µM PMSF, 1 µg/ml pepstatin A, 1× protease inhibitor (Roche) and 1× PhosSTOP phosphatase inhibitor (Roche)] before being resuspended and set on ice for another 10 min. Cells were then spun down at 17,000 ***g*** for 1 min to collect the supernatant cytoplasmic fraction. The pellet was then washed three times in PBS with spinning at 17,000 ***g*** for 1 min in between washes to remove any residual cytoplasmic components. The pellet was then resuspended in nuclear lysis buffer [50 mM Tris-HCl pH 7.4, 300 mM NaCl, 0.3% Triton X-100, 50 mM N-acetylglucosamine, 1 mM DTT, 100 µM PMSF, 1 µg/ml pepstain A, 1× protease inhibitor (Roche) and 1× PhosSTOP phosphatase inhibitor (Roche)] before vortexing to release nuclear contents. Nuclear fractions were additionally sonicated 20 times in 0.5 s bursts to liberate dense nuclear aggregates. Cytoplasmic and nuclear fractions were analyzed by SDS-PAGE. Protein concentrations were determined using a Bradford assay, and equal amounts of protein were loaded on gels before running in a Laemmli buffer. Proteins were transferred to a nitrocellulose membrane (BioRad) by wet transfer at 4°C. The membrane was then rinsed with Tris-buffered saline (TBS, pH 7.5) and blocked with 5% milk in TBS for 1 h. Membranes were probed with the following primary antibodies: mouse anti-lamin A/C (1:1000, Santa Cruz Biotechnology, sc-7292), mouse anti-actin (1:1000, Santa Cruz Biotechnology, sc-8432), mouse anti-BAF (1:1000, Santa Cruz Biotechnology, sc-166324), rabbit anti-SUN1 (1:2000; HPA008346, Sigma-Aldrich), mouse anti-histone H2A (1:1000, Santa Cruz Biotechnology, sc-515808) and mouse anti-GAPDH (1:1000, GeneTex, GTX627408). A goat anti-mouse-IgG (H+L) HRP conjugate (1:3000, Invitrogen, 62-6520) and a goat anti-rabbit-IgG (H+L) HRP conjugate (1:5000, Invitrogen, 65-6120) were used as secondary antibodies. Blots were developed with SuperSignal West Femto Maximum Sensitivity Substrate (Thermo Fisher Scientific) and imaged on a Chemidoc XRS+ (BioRad). All assays were performed in triplicate and immunoblot quantification was done with ImageJ, using two-tailed unpaired *t*-tests for statistical comparisons with wild-type (Fig. S2).

Immunostaining and fluorescence imaging of RNAi effects and exogenous protein expressions

EMD$^{+/y}$ HDFs were transfected with control siRNAs, or siRNAs against lamin A/C, IPO9, BAF, and SUN1, respectively as described above. Cells were fixed with 4% PFA in 1× PBS for 15 min, permeabilized with 0.1% Triton X-100 for 10 min, and blocked with 4% BSA and 0.1% Tween 20 for 1 h, all at room temperature. For lamin A/C and SUN1 immunostaining, cells were incubated with mouse anti-lamin A/C (1:400; sc-7292, Santa Cruz Biotechnology) and rabbit anti-SUN1 (1:500; HPA008346, Sigma-Aldrich) for 1 h at room temperature, rinsed three times with 1× PBS for 5 min each, then stained with goat anti-mouse-Alexa Fluor 647 (1:500, Life Technologies) and goat anti-rabbit-Alexa Fluor 488 (1:500, Life Technologies) for 1 h at room temperature. Following three PBS rinses, the coverslips were mounted in DAPI-Fluoromount G (Electron Microscopy Sciences) and imaged. For BAF staining, cells were incubated with mouse anti-BAF (1:100; sc-166324, Santa Cruz Biotechnology) for 2 h at room temperature, then with goat anti-mouse-Alexa Fluor 647 (1:500) for further 2 h. To assess the effect of BAF L58R re-expression on lamin A/C organization, 24 h after siRNA treatment against BAF, cells were transduced with the lentivirus for EGFP-BAF L58R expression and fixed 2 days later, before staining for lamin A/C as described above. To assess the influence of lamin A/C or EGFP-SUN1 expression on the localization of endogenous emerin, *EMD*$^{+/y}$ HDFs were fixed and immunostained with rabbit anti-emerin (1 µg/ml; cat. no. ab40688, Abcam) and mouse anti-lamin A/C (1:400; cat. no. sc-7292, Santa Cruz Biotechnology) antibodies as described above. Confocal fluorescence imaging (Figs S2 and S6) was performed on a Zeiss LSM 780 microscope equipped with a C-Apochromat 63×/1.15 W Korr objective, excitation lasers at 405 nm, 488 nm and 633 nm, and appropriate beam splitter and emission channel settings for detection of DAPI, GFP, and Alexa Fluor 488- and Alexa Fluor 647-labeled secondary antibodies. Other than effective and specific knockdown of targeted protein expressions, there were no obvious indirect or off-target effects of the different siRNA treatments on the organization of other studied proteins (Fig. S2).

To assess the influence of IPO9 and XPO6 siRNA on nuclear actin organization and content, Utr230-EGFP-3xNLS (Utr230-EN, Addgene #58466) was subcloned into a pHR-SFFV lentiviral plasmid backbone, viral particles were generated, and *EMD*$^{+/y}$ HDF cells were transduced with 25 ng ml^{-1} of lentiviral particles as described for SNAP–emerin. 10 µg/ml blasticidin S (InvivoGen) was used over 12 days to establish a stable cell line expressing Utr230-EN. Cells were then transfected with 25 nM of control, IPO9 or XPO6 siRNAs, as described above, before being fixed with 4% PFA for 15 min, rinsed three times with 1× PBS, and mounted using Fluoromount-G (Electron Microscopy Sciences). Confocal fluorescence imaging was performed on a Zeiss LSM 780 upright microscope equipped with a Plan-Apochromat 40×/1.4 Oil objective, excitation laser at 488 nm, and appropriate beam splitter and emission channel settings for the detection of EGFP. From confocal images, cells were classified into three groups depending on the nuclear localization pattern of Utr230-EN: (1) small puncta and diffuse, (2) diffuse or (3) large foci, based on a similar previous classification (Belin et al., 2013). Data were pooled from three independent assays for each condition.

Quantification of ONM emerin fraction

The fraction of ONM emerin in *EMD*$^{+/y}$ HDFs was quantified after saponin (ONM+ER emerin) or Triton X-100 (INM+ONM+ER emerin) permeabilization and immunostaining with rabbit anti-emerin (1 µg/ml, ab40688, Abcam) and mouse anti-lamin A/C (1:1000, sc-7292, Santa Cruz Biotechnology) antibodies, as previously described (Bautista et al., 2019). Whole-cell volumes were imaged by 3D confocal microscopy and all the *z*-

slices were combined into a single image by sum intensity *z*-slices projection. Regions of interest (ROIs) were delineated to quantify emerin fluorescence intensities over the entire cells (ROI1) or over the nucleus (ROI2) after background corrections. Nuclear ROI2 were further corrected for ER emerin contributions by evaluating the mean ER-only emerin intensity per area from ROI1−ROI2 intensities. Using a representative set of 20 cells for both saponin and Triton X-100 treatments, the fraction of ONM emerin per cell was then calculated using: ONM fraction=$ER_{corrected}$ $ROI2_{saponin(ONM)}$/$ER_{corrected}$ $ROI2_{Triton\ X-100(INM+ONM)}$. The mean ONM fraction of emerin at the NE was 13±6%, in good agreement with the levels of ONM emerin detected in sptPALM experiments (Fig. S4).

Analyses of diffusion coefficients

Localization and tracking analyses were performed using the software package SLIMfast, which uses multiple-target tracing algorithms (Serge et al., 2008) and was kindly provided by Christian Ritcher and Jacob Piehler. Localizations were performed by 2D-gaussian fitting of the point spread function of each activated PA-TagRFP–emerin or activated emerin–GFP–emerin species in each frame. Localization precision was determined as previously described (Mortensen et al., 2010; Thompson et al., 2002), and individual PA-TagRFP–emerin molecules were localized with a precision of 13±5 nm. Diffusion trajectories were built by linking localizations frame to frame and accounting for blinking statistics and local particle densities. Trajectories with fewer than three steps were discarded. Diffusion coefficients were estimated using a probability density of square displacement (PDSD) analysis (Schutz et al., 1997). For each time lag *t*, the PDSD curve was fitted with the following model:

$$P(\vec{r}^2,t) = 1 - \sum_{i=1}^{n} a_i(t) e^{-r^2/r_i^2(t)} \qquad (2)$$

$$\sum_{i=1}^{n} a_i(t) = 1,$$

where $r_i^2(t)$ is the square displacement and $a_i(t)$ is the population density of *i* numbers of diffusive behaviors at each time lag *t*. To limit the risks of overfitting or underfitting the PDSD curves and select an appropriate model for *i* numbers of diffusive behaviors in each data set, we used both an Akaike information criterion (AIC) and a Bayesian information criterion (BIC) after fitting PDSD with models where $1 \leq i \geq 5$. Square displacement curves [$r_i^2(t)$] were extracted from PDSD analyses and reported with error bars determined using $\frac{r_i^2}{\sqrt{N}}$, where N is the number of analyzed trajectories per time lag, as previously described (Schutz et al., 1997). Diffusion coefficients (*D*) representative of each behavior were determined by fitting each $r_i^2(t)$ curves over the first four time lags (t_1-t_4) using OriginPro 2020 software (OriginLab) and a 2D Brownian diffusion model with position error:

$$r^2 = 4Dt + 4\sigma^2. \qquad (3)$$

The numbers of trajectories and nuclei analyzed were: wild-type emerin (71,004 trajectories, 14 nuclei); lamin A/C depletion (lamin A/C KD, 60,569 trajectories, 11 nuclei); nuclear actin depletion (IPO9 KD, 74501 trajectories, 17 nuclei); replacement of endogenous BAF with BAF^{L58R} (BAF KD+BAF^{L58R}, 62,714 trajectories, 8 nuclei); complemented wild-type emerin–GFP–emerin species assessed by CALM (4833 trajectories, 13 nuclei); wild-type emerin after nuclear deformation on 15 µm (27,266 trajectories, 10 nuclei); wild-type emerin after nuclear deformation on 10 µm wide micropatterns (12,915 trajectories, 8 nuclei); Q133H emerin (105,050 trajectories, 13 nuclei); Δ95-99 emerin (76,944 trajectories,14 nuclei); P183H emerin (86,529 trajectories, 21 nuclei); and complemented P183H emerin–GFP–emerin species assessed by CALM (10,519 trajectories, 21 nuclei). All diffusion coefficients *D* are reported in $\mu m^2\ s^{-1}$ of fit value (mean±s.e.m.). Statistical comparisons between *D* values were done using two-tailed unpaired *t*-tests. Population percentages are derived from the averaged $a_i(t)$ values over the considered time lags.

To estimate the diffusion that might be expected for immobile PA-TagRFP–emerin ($D_{immobile}$) under our imaging and analytical conditions, we simulated immobilized PA-TagRFP emerin with photophysical parameters similar to that of live cell acquisitions, using the software Fluosim (Lagardère et al., 2020). After PDSD analysis with SLIMfast, $D_{immobile}$ was determined at $1.7\times10^{-4}\pm2\times10^{-5}$ $\mu m^2\ s^{-1}$.

Individual diffusion coefficients (D_i) were obtained by fitting the individual mean square displacement (MSD) for each detected emerin over the first three time lags (t_1-t_3), using again a 2D Brownian diffusion model. Based on their individual D_i value, emerin trajectories were grouped into four diffusion ranges (D_{i1}>0.1 $\mu m^2\ s^{-1}$, 0.1<D_{i2}>0.01 $\mu m^2\ s^{-1}$, 0.1<D_{i3}> 0.001 $\mu m^2\ s^{-1}$, and D_{i4}< 0.001 $\mu m^2\ s^{-1}$) and plotted as maps.

Spatial distribution and cluster analyses from super-resolution images

After 3D-dSTORM super-resolution imaging, the localization of individual emerin molecules and *z*-position assignments were performed by Gaussian fitting using rapidSTORM (version 3.3.1) (Wolter et al., 2012). Sample drift and overcounting corrections for molecules appearing in consecutive frames were done using PALMsiever (Pengo et al., 2015) and renderings of super-resolved images were done using ImageJ. Localization precisions (σ) in the *x*, *y* and *z* dimensions were evaluated as previously described (Fernandez et al., 2017) and were σ_x, 8.3 nm; σ_y, 13.0 nm; and σ_z, 28.4 nm. 2D spatial pattern analyses of emerin distributions were performed on 2 µm×2 µm ROIs typically chosen in NE areas having homogenous *z* ranges and away from the edges of nuclei, in order to limit 3D effects.

Emerin clustering was determined using an edge-corrected NDF as previously described (Fernandez et al., 2017). Briefly, the NDF is a pairwise-correlation function similar to O-ring statistics that tallies the density of detected emerin within a ring of outer radius *r* and width *Δr* located at a distance *r* from an emerin position in the ROI and for all *r*+*Δr* in the ROI. The density of emerin as a function of distance from an average emerin was obtained with:

$$D_r = \frac{\sum N_r}{\sum A_r}, \qquad (4)$$

where N_r is the number of neighbors and A_r is the area summed over all detected emerin. NDF analyses were done over a 1 µm distance on selected ROIs and with a fixed ring width of 10 nm and a ring radius increasing by 10 nm steps. To average NDF statistics from multiple ROIs across different nuclei and make them sample-size independent, D_r was further standardized by dividing it by the mean density of detected emerin across the entire ROI. As such, an NDF value at a given radius indicates the relative clustering of emerin as compared to the average density across the entire sample. This relative NDF gives a value of 1 for a completely random spatial distribution as determined by Monte Carlo simulations of random emerin distributions with area and number of randomly seeded emerin equal to that of each experimental ROIs.

Relative NDF curves averaged across multiple ROIs and multiple nuclei were fitted with a previously described model (Fernandez et al., 2017), which accounts for a distribution of cluster lengths that includes two populations of emerin (monomer and oligomers) and for a probability density of emerin in 2D clusters that decays approximately as an exponential function (Sengupta et al., 2011):

$$\text{Relative NDF} = \{A_1 \times \exp\left(\frac{-r}{\varepsilon_1}\right) + A_2 \times \exp\left(\frac{-r}{\varepsilon_2}\right) + 1\} * g(r)^{PSF}, \qquad (5)$$

where *A* is the clustering density, ε is the typical half-maximum cluster length, * denotes a 2D convolution, and $g(r)^{PSF}$ is the correlation function of the effective point spread function of uncertainty in position determination for the dSTORM experiments. As described previously (Fernandez et al., 2017), $g(r)^{PSF}$ corrects the NDF for contribution of multiple single-molecule appearances (blinking) to the overall spatial distribution. After fitting relative NDF curves, the molecular density above random for emerin clusters are reported as *A* ±s.e. of the fit (±s.e.m.) and their typical size as 2×ε ±s.e. of the fit and localization precision (±s.e.m.). Relative increases in emerin oligomer formation during nuclear stress were determined by considering a circular shape of oligomer nanodomains and multiplying the area of oligomerization by the measured molecular density.

The numbers of localization and nuclei analyzed were: wild-type emerin in untreated cells (189,331 localizations, 10 nuclei); after control siRNA transfection (n=180,546 localizations, 5 nuclei); after lamin A/C knockdown (178,206 localizations, 6 nuclei); after lamin A/C knockdown and exogenous expression of lamin A/C (118,859 localizations, 6 nuclei); after IPO9 knockdown (225,394 localizations, 9 nuclei); after replacement of endogenous BAF by BAF^{L58R} (90,241 localizations, 6 nuclei); after SUN1 knockdown (258,300 localizations, 6 nuclei); after SUN1 knockdown and exogenous expression of EGFP-SUN1 (85,210 localizations, 5 nuclei); after exogenous expression of mCherry-DN-KASH (392,365 localizations, 5 nuclei); after nuclear deformation on 15 µm wide micropatterns (151,647 localizations, 10 nuclei); after nuclear deformation on 10 µm wide micropatterns (56,563 localizations, 6 nuclei); for Q133H emerin (149,340 localizations, 6 nuclei); for Δ95-99 emerin (208,092 localizations, 8 nuclei); for P183H emerin (138,075 localizations, 6 nuclei); for Δ95-99 emerin after nuclear deformation on 15 µm wide micropatterns (138,119 localizations, 5 nuclei); and for Δ95-99 emerin after nuclear deformation on 10 µm wide micropatterns (135,143 localizations, 6 nuclei).

Cluster maps

Cluster maps were generated from drift- and overcounting-corrected super-resolved emerin positions by determining local cluster values around each emerin using the Getis and Franklin L function (Getis and Franklin, 1987) in spPack (Perry, 2004) and for a distance of 25 nm. Spatial positions in x and y, and cluster values were plotted as maps in MATLAB (MathWorks) using the meshgrid and griddata functions, a 1 nm×1 nm pixel size and the 'v4' option when calculating pixel density values. The contour maps were generated using the countourf function with 200 levels. In contour maps, values $L(r_{25})$=25 represent areas where emerin is randomly distributed and $L(r_{25})$=70 values represent areas with emerin local density $(70/25)^2$=∼8-fold higher than expected for a random distribution.

Acknowledgements

We are grateful to H. Worman for providing emerin null and normal HDFs and to J. Ellis, R. Frock and C. Doucet for providing emerin, lamin A/C and EGFP-SUN1 cDNAs, respectively.

Competing interests

The authors declare no competing or financial interests.

Author contributions

Conceptualization: A.F., M.B., L.W., F.P.; Methodology: A.F., M.B., L.W., F.P.; Validation: A.F., M.B., L.W., F.P.; Formal analysis: A.F., M.B., L.W., F.P.; Investigation: A.F., M.B., L.W., F.P.; Resources: A.F., M.B., L.W.; Writing - original draft: F.P.; Writing - review & editing: F.P.; Visualization: A.F., F.P.; Supervision: F.P.; Project administration: F.P.; Funding acquisition: F.P.

Funding

This work was supported by the National Institute of Arthritis and Musculoskeletal and Skin Diseases of the National Institutes of Health under award number R21AR076514. Deposited in PMC for release after 12 months.

Peer review history

The peer review history is available online at https://journals.biologists.com/jcs/article-lookup/doi/10.1242/jcs.258969.

References

Arsenovic, P. T., Ramachandran, I., Bathula, K., Zhu, R., Narang, J. D., Noll, N. A., Lemmon, C. A., Gundersen, G. G. and Conway, D. E. (2016). Nesprin-2G, a component of the nuclear LINC complex, is subject to myosin-dependent tension. *Biophys. J.* **110**, 34-43. doi:10.1016/j.bpj.2015.11.014

Baarlink, C., Plessner, M., Sherrard, A., Morita, K., Misu, S., Virant, D., Kleinschnitz, E. M., Harniman, R., Alibhai, D., Baumeister, S. et al. (2017). A transient pool of nuclear F-actin at mitotic exit controls chromatin organization. *Nat. Cell Biol.* **19**, 1389-1399. doi:10.1038/ncb3641

Bautista, M., Fernandez, A. and Pinaud, F. (2019). A micropatterning strategy to study nuclear mechanotransduction in cells. *Micromachines (Basel)* **10**, 810.

Belin, B. J., Cimini, B. A., Blackburn, E. H. and Mullins, R. D. (2013). Visualization of actin filaments and monomers in somatic cell nuclei. *Mol. Biol. Cell* **24**, 982-994. doi:10.1091/mbc.e12-09-0685

Bengtsson, L. and Wilson, K. L. (2004). Multiple and surprising new functions for emerin, a nuclear membrane protein. *Curr. Opin. Cell Biol.* **16**, 73-79. doi:10.1016/j.ceb.2003.11.012

Berk, J. M., Maitra, S., Dawdy, A. W., Shabanowitz, J., Hunt, D. F. and Wilson, K. L. (2013a). O-Linked beta-N-acetylglucosamine (O-GlcNAc) regulates emerin binding to barrier to autointegration factor (BAF) in a chromatin- and lamin B-enriched "niche". *J. Biol. Chem.* **288**, 30192-30209. doi:10.1074/jbc.M113.503060

Berk, J. M., Tifft, K. E. and Wilson, K. L. (2013b). The nuclear envelope LEM-domain protein emerin. *Nucleus* **4**, 298-314. doi:10.4161/nucl.25751

Berk, J. M., Simon, D. N., Jenkins-Houk, C. R., Westerbeck, J. W., Gronning-Wang, L. M., Carlson, C. R. and Wilson, K. L. (2014). The molecular basis of emerin-emerin and emerin-BAF interactions. *J. Cell Sci.* **127**, 3956-3969.

Burger, M., Schmitt-Koopmann, C. and Leroux, J.-C. (2020). DNA unchained: two assays to discover and study inhibitors of the DNA clustering function of barrier-to-autointegration factor. *Sci. Rep.* **10**, 12301. doi:10.1038/s41598-020-69246-x

Clements, L., Manilal, S., Love, D. R. and Morris, G. E. (2000). Direct interaction between emerin and lamin A. *Biochem. Biophys. Res. Commun.* **267**, 709-714. doi:10.1006/bbrc.1999.2023

Crisp, M., Liu, Q., Roux, K., Rattner, J. B., Shanahan, C., Burke, B., Stahl, P. D. and Hodzic, D. (2006). Coupling of the nucleus and cytoplasm: role of the LINC complex. *J. Cell Biol.* **172**, 41-53. doi:10.1083/jcb.200509124

Cui, Y., Hameed, F. M., Yang, B., Lee, K., Pan, C. Q., Park, S. and Sheetz, M. (2015). Cyclic stretching of soft substrates induces spreading and growth. *Nat. Commun.* **6**, 6333. doi:10.1038/ncomms7333

Demmerle, J., Koch, A. J. and Holaska, J. M. (2012). The nuclear envelope protein emerin binds directly to histone deacetylase 3 (HDAC3) and activates HDAC3 activity. *J. Biol. Chem.* **287**, 22080-22088. doi:10.1074/jbc.M111.325308

Dopie, J., Skarp, K. P., Rajakyla, E. K., Tanhuanpaa, K. and Vartiainen, M. K. (2012). Active maintenance of nuclear actin by importin 9 supports transcription. *Proc. Natl. Acad. Sci. U.S.A.* **109**, E544-E552.

Emery, A. E. and Dreifuss, F. E. (1966). Unusual type of benign x-linked muscular dystrophy. *J. Neurol. Neurosurg. Psychiatry* **29**, 338-342. doi:10.1136/jnnp.29.4.338

Fairley, E. A., Kendrick-Jones, J. and Ellis, J. A. (1999). The Emery-Dreifuss muscular dystrophy phenotype arises from aberrant targeting and binding of emerin at the inner nuclear membrane. *J. Cell Sci.* **112**, 2571-2582. doi:10.1242/jcs.112.15.2571

Fernandez, A., Bautista, M., Stanciauskas, R., Chung, T. and Pinaud, F. (2017). Cell-shaping micropatterns for quantitative super-resolution microscopy imaging of membrane mechanosensing proteins. *ACS Appl. Mater. Interfaces* **9**, 27575-27586. doi:10.1021/acsami.7b09743

Fidzianska, A. and Hausmanowa-Petrusewicz, I. (2003). Architectural abnormalities in muscle nuclei. Ultrastructural differences between X-linked and autosomal dominant forms of EDMD. *J. Neurol. Sci.* **210**, 47-51.

Frock, R. L., Kudlow, B. A., Evans, A. M., Jameson, S. A., Hauschka, S. D. and Kennedy, B. K. (2006). Lamin A/C and emerin are critical for skeletal muscle satellite cell differentiation. *Genes Dev.* **20**, 486-500. doi:10.1101/gad.1364906

Getis, A. and Franklin, J. (1987). Second-order neighborhood analysis of mapped point patterns. *Ecology* **68**, 473-477. doi:10.2307/1938452

Guilluy, C., Osborne, L. D., Van Landeghem, L., Sharek, L., Superfine, R., Garcia-Mata, R. and Burridge, K. (2014). Isolated nuclei adapt to force and reveal a mechanotransduction pathway in the nucleus. *Nat. Cell Biol.* **16**, 376-381. doi:10.1038/ncb2927

Haque, F., Lloyd, D. J., Smallwood, D. T., Dent, C. L., Shanahan, C. M., Fry, A. M., Trembath, R. C. and Shackleton, S. (2006). SUN1 interacts with nuclear lamin A and cytoplasmic nesprins to provide a physical connection between the nuclear lamina and the cytoskeleton. *Mol. Cell. Biol.* **26**, 3738-3751. doi:10.1128/MCB.26.10.3738-3751.2006

Haque, F., Mazzeo, D., Patel, J. T., Smallwood, D. T., Ellis, J. A., Shanahan, C. M. and Shackleton, S. (2010). Mammalian SUN protein interaction networks at the inner nuclear membrane and their role in laminopathy disease processes. *J. Biol. Chem.* **285**, 3487-3498. doi:10.1074/jbc.M109.071910

Haraguchi, T., Kojidani, T., Koujin, T., Shimi, T., Osakada, H., Mori, C., Yamamoto, A. and Hiraoka, Y. (2008). Live cell imaging and electron microscopy reveal dynamic processes of BAF-directed nuclear envelope assembly. *J. Cell Sci.* **121**, 2540-2554. doi:10.1242/jcs.033597

Hennen, J., Saunders, C. A., Mueller, J. D. and Luxton, G. W. G. (2018). Fluorescence fluctuation spectroscopy reveals differential SUN protein oligomerization in living cells. *Mol. Biol. Cell* **29**, 1003-1011.

Herrada, I., Samson, C., Velours, C., Renault, L., Ostlund, C., Chervy, P., Puchkov, D., Worman, H. J., Buendia, B. and Zinn-Justin, S. (2015). Muscular dystrophy mutations impair the nuclear envelope emerin self-assembly properties. *ACS Chem. Biol.* **10**, 2733-2742. doi:10.1021/acschembio.5b00648

Hirano, Y., Segawa, M., Ouchi, F. S., Yamakawa, Y., Furukawa, K., Takeyasu, K. and Horigome, T. (2005). Dissociation of emerin from barrier-to-autointegration factor is regulated through mitotic phosphorylation of emerin in a xenopus egg cell-free system*. *J. Biol. Chem.* **280**, 39925-39933. doi:10.1074/jbc.M503214200

Ho, C. Y., Jaalouk, D. E., Vartiainen, M. K. and Lammerding, J. (2013). Lamin A/C and emerin regulate MKL1–SRF activity by modulating actin dynamics. *Nature* **497**, 507-511. doi:10.1038/nature12105

Holaska, J. M., Kowalski, A. K. and Wilson, K. L. (2004). Emerin caps the pointed end of actin filaments: evidence for an actin cortical network at the nuclear inner membrane. *PLoS Biol.* **2**, E231. doi:10.1371/journal.pbio.0020231

Holt, I., Clements, L., Manilal, S. and Morris, G. E. (2001). How does a g993t mutation in the emerin gene cause Emery-Dreifuss muscular dystrophy? *Biochem. Biophys. Res. Commun.* **287**, 1129-1133. doi:10.1006/bbrc.2001.5708

Jahed, Z., Fadavi, D., Vu, U. T., Asgari, E., Luxton, G. W. G. and Mofrad, M. R. K. (2018). Molecular insights into the mechanisms of SUN1 oligomerization in the nuclear envelope. *Biophys. J.* **114**, 1190-1203. doi:10.1016/j.bpj.2018.01.015

Kirby, T. J. and Lammerding, J. (2018). Emerging views of the nucleus as a cellular mechanosensor. *Nat. Cell Biol.* **20**, 373-381. doi:10.1038/s41556-018-0038-y

Lagardère, M., Chamma, I., Bouilhol, E., Nikolski, M. and Thoumine, O. (2020). FluoSim: simulator of single molecule dynamics for fluorescence live-cell and super-resolution imaging of membrane proteins. *Sci. Rep.* **10**, 19954. doi:10.1038/s41598-020-75814-y

Lammerding, J., Hsiao, J., Schulze, P. C., Kozlov, S., Stewart, C. L. and Lee, R. T. (2005). Abnormal nuclear shape and impaired mechanotransduction in emerin-deficient cells. *J. Cell Biol.* **170**, 781-791. doi:10.1083/jcb.200502148

Lee, K. K., Haraguchi, T., Lee, R. S., Koujin, T., Hiraoka, Y. and Wilson, K. L. (2001). Distinct functional domains in emerin bind lamin A and DNA-bridging protein BAF. *J. Cell Sci.* **114**, 4567-4573. doi:10.1242/jcs.114.24.4567

Loi, M., Cenni, V., Duchi, S., Squarzoni, S., Lopez-Otin, C., Foisner, R., Lattanzi, G. and Capanni, C. (2016). Barrier-to-autointegration factor (BAF) involvement in prelamin A-related chromatin organization changes. *Oncotarget* **7**, 15662-15677. doi:10.18632/oncotarget.6697

Lombardi, M. L., Jaalouk, D. E., Shanahan, C. M., Burke, B., Roux, K. J. and Lammerding, J. (2011). The interaction between nesprins and sun proteins at the nuclear envelope is critical for force transmission between the nucleus and cytoskeleton. *J. Biol. Chem.* **286**, 26743-26753. doi:10.1074/jbc.M111.233700

Lu, W., Gotzmann, J., Sironi, L., Jaeger, V. M., Schneider, M., Lüke, Y., Uhlén, M., Szigyarto, C. A., Brachner, A., Ellenberg, J. et al. (2008). Sun1 forms immobile macromolecular assemblies at the nuclear envelope. *Biochim. Biophys. Acta* **1783**, 2415-2426.

Maurer, M. and Lammerding, J. (2019). The driving force: nuclear mechanotransduction in cellular function, fate, and disease. *Annu. Rev. Biomed. Eng.* **21**, 443-468. doi:10.1146/annurev-bioeng-060418-052139

Mislow, J. M. K., Holaska, J. M., Kim, M. S., Lee, K. K., Segura-Totten, M., Wilson, K. L. and McNally, E. M. (2002). Nesprin-1α self-associates and binds directly to emerin and lamin A in vitro. *FEBS Lett.* **525**, 135-140. doi:10.1016/S0014-5793(02)03105-8

Mortensen, K. I., Churchman, L. S., Spudich, J. A. and Flyvbjerg, H. (2010). Optimized localization analysis for single-molecule tracking and super-resolution microscopy. *Nat. Methods* **7**, 377-381. doi:10.1038/nmeth.1447

Ostlund, C., Ellenberg, J., Hallberg, E., Lippincott-Schwartz, J. and Worman, H. J. (1999). Intracellular trafficking of emerin, the Emery-Dreifuss muscular dystrophy protein. *J. Cell Sci.* **112**, 1709-1719.

Ostlund, C., Sullivan, T., Stewart, C. L. and Worman, H. J. (2006). Dependence of diffusional mobility of integral inner nuclear membrane proteins on A-type lamins. *Biochemistry* **45**, 1374-1382. doi:10.1021/bi052156n

Pengo, T., Holden, S. J. and Manley, S. (2015). PALMsiever: a tool to turn raw data into results for single-molecule localization microscopy. *Bioinformatics* **31**, 797-798. doi:10.1093/bioinformatics/btu720

Perry, G. L. W. (2004). SpPack: spatial point pattern analysis in Excel using Visual Basic for Applications (VBA). *Environ. Model. Softw.* **19**, 559-569.

Phair, R. D., Gorski, S. A. and Misteli, T. (2004). Measurement of dynamic protein binding to chromatin in vivo, using photobleaching microscopy. *Methods Enzymol.* **375**, 393-414. doi:10.1016/S0076-6879(03)75025-3

Pinaud, F. and Dahan, M. (2011). Targeting and imaging single biomolecules in living cells by complementation-activated light microscopy with split-fluorescent proteins. *Proc. Natl Acad. Sci. USA* **108**, E201-E210.

Roberts, R. C., Sutherland-Smith, A. J., Wheeler, M. A., Jensen, O. N., Emerson, L. J., Spiliotis, I. I., Tate, C. G., Kendrick-Jones, J. and Ellis, J. A. (2006). The Emery-Dreifuss muscular dystrophy associated-protein emerin is phosphorylated on serine 49 by protein kinase A. *FEBS J.* **273**, 4562-4575. doi:10.1111/j.1742-4658.2006.05464.x

Rowat, A. C., Lammerding, J. and Ipsen, J. H. (2006). Mechanical properties of the cell nucleus and the effect of emerin deficiency. *Biophys. J.* **91**, 4649-4664. doi:10.1529/biophysj.106.086454

Sakaki, M., Koike, H., Takahashi, N., Sasagawa, N., Tomioka, S., Arahata, K. and Ishiura, S. (2001). Interaction between emerin and nuclear lamins. *J. Biochem.* **129**, 321-327. doi:10.1093/oxfordjournals.jbchem.a002860

Salpingidou, G., Smertenko, A., Hausmanowa-Petrucewicz, I., Hussey, P. J. and Hutchison, C. J. (2007). A novel role for the nuclear membrane protein emerin in association of the centrosome to the outer nuclear membrane. *J. Cell Biol.* **178**, 897-904. doi:10.1083/jcb.200702026

Samson, C., Celli, F., Hendriks, K., Zinke, M., Essawy, N., Herrada, I., Arteni, A. A., Theillet, F. X., Alpha-Bazin, B., Armengaud, J. et al. (2017). Emerin self-assembly mechanism: role of the LEM domain. *FEBS J.* **284**, 338-352. doi:10.1111/febs.13983

Samson, C., Petitalot, A., Celli, F., Herrada, I., Ropars, V., Le Du, M. H., Nhiri, N., Jacquet, E., Arteni, A. A., Buendia, B. et al. (2018). Structural analysis of the ternary complex between lamin A/C, BAF and emerin identifies an interface disrupted in autosomal recessive progeroid diseases. *Nucleic Acids Res.* **46**, 10460-10473. doi:10.1093/nar/gky736

Samwer, M., Schneider, M. W. G., Hoefler, R., Schmalhorst, P. S., Jude, J. G., Zuber, J. and Gerlich, D. W. (2017). DNA cross-bridging shapes a single nucleus from a set of mitotic chromosomes. *Cell* **170**, 956-972.

Schneider, C. A., Rasband, W. S. and Eliceiri, K. W. (2012). NIH Image to ImageJ: 25 years of image analysis. *Nat. Methods* **9**, 671-675. doi:10.1038/nmeth.2089

Schutz, G. J., Schindler, H. and Schmidt, T. (1997). Single-molecule microscopy on model membranes reveals anomalous diffusion. *Biophys. J.* **73**, 1073-1080. doi:10.1016/S0006-3495(97)78139-6

Sengupta, P., Jovanovic-Talisman, T., Skoko, D., Renz, M., Veatch, S. L. and Lippincott-Schwartz, J. (2011). Probing protein heterogeneity in the plasma membrane using PALM and pair correlation analysis. *Nat. Methods* **8**, 969-975.

Serge, A., Bertaux, N., Rigneault, H. and Marguet, D. (2008). Dynamic multiple-target tracing to probe spatiotemporal cartography of cell membranes. *Nat. Methods* **5**, 687-694. doi:10.1038/nmeth.1233

Shimi, T., Koujin, T., Segura-Totten, M., Wilson, K. L., Haraguchi, T. and Hiraoka, Y. (2004). Dynamic interaction between BAF and emerin revealed by FRAP, FLIP, and FRET analyses in living HeLa cells. *J. Struct. Biol.* **147**, 31-41. doi:10.1016/j.jsb.2003.11.013

Soumpasis, D. M. (1983). Theoretical analysis of fluorescence photobleaching recovery experiments. *Biophys. J.* **41**, 95-97. doi:10.1016/S0006-3495(83)84410-5

Stephens, A. D., Banigan, E. J., Adam, S. A., Goldman, R. D. and Marko, J. F. (2017). Chromatin and lamin A determine two different mechanical response regimes of the cell nucleus. *Mol. Biol. Cell* **28**, 1984-1996. doi:10.1091/mbc.e16-09-0653

Stoynova, L., Solórzano, R. and Collins, E. D. (2004). Generation of large deletion mutants from plasmid DNA. *BioTechniques* **36**, 402-406.

Subach, F. V., Patterson, G. H., Renz, M., Lippincott-Schwartz, J. and Verkhusha, V. V. (2010). Bright monomeric photoactivatable red fluorescent protein for two-color super-resolution sptPALM of live cells. *J. Am. Chem. Soc.* **132**, 6481-6491.

Talamas, J. A. and Hetzer, M. W. (2011). POM121 and Sun1 play a role in early steps of interphase NPC assembly. *J. Cell Biol.* **194**, 27-37. doi:10.1083/jcb.201012154

Talkop, U. A., Talvik, I., Sõnajalg, M., Sibul, H., Kolk, A., Piirsoo, A., Warzok, R., Wulff, K., Wehnert, M. S. and Talvik, T. (2002). Early onset of cardiomyopathy in two brothers with X-linked Emery-Dreifuss muscular dystrophy. *Neuromuscul. Disord.* **12**, 878-881. doi:10.1016/S0960-8966(02)00134-7

Thompson, R. E., Larson, D. R. and Webb, W. W. (2002). Precise nanometer localization analysis for individual fluorescent probes. *Biophys. J.* **82**, 2775-2783. doi:10.1016/S0006-3495(02)75618-X

Tifft, K. E., Bradbury, K. A. and Wilson, K. L. (2009). Tyrosine phosphorylation of nuclear-membrane protein emerin by Src, Abl and other kinases. *J. Cell Sci.* **122**, 3780-3790. doi:10.1242/jcs.048397

Tokunaga, M., Imamoto, N. and Sakata-Sogawa, K. (2008). Highly inclined thin illumination enables clear single-molecule imaging in cells. *Nat. Methods* **5**, 159-161. doi:10.1038/nmeth1171

van de Linde, S., Löschberger, A., Klein, T., Heidbreder, M., Wolter, S., Heilemann, M. and Sauer, M. (2011). Direct stochastic optical reconstruction microscopy with standard fluorescent probes. *Nat. Protoc.* **6**, 991-1009. doi:10.1038/nprot.2011.336

Wolter, S., Loschberger, A., Holm, T., Aufmkolk, S., Dabauvalle, M. C., van de Linde, S. and Sauer, M. (2012). rapidSTORM: accurate, fast open-source software for localization microscopy. *Nat. Methods* **9**, 1040-1041. doi:10.1038/nmeth.2224

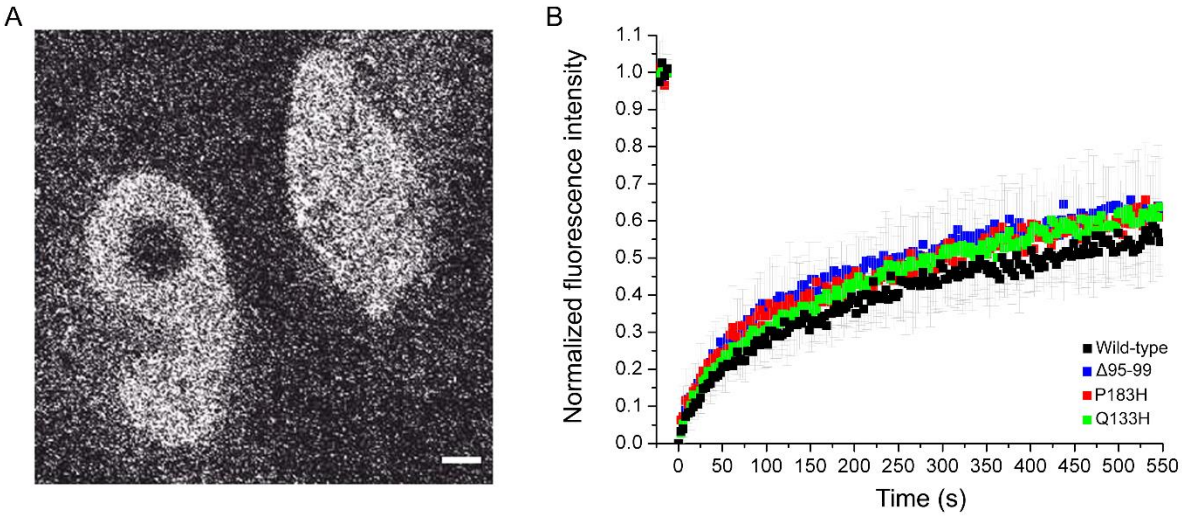

C

	D_{fast} ($\mu m^2/s$)	D_{fast} (%)	D_{slow} ($\mu m^2/s$)	D_{slow} (%)
Wildtype	$4.48x10^{-2} \pm 1x10^{-2}$	17	$4.0x10^{-3} \pm 4x10^{-4}$	83
P183H	$7.73x10^{-2} \pm 2x10^{-2}$	17	$5.0x10^{-3} \pm 5x10^{-4}$	83
Q133H	$9.97x10^{-2} \pm 3x10^{-2}$	9	$6.7x10^{-3} \pm 3x10^{-4}$	91
Δ95-99	$5.22x10^{-2} \pm 1x10^{-2}$	32	$4.7x10^{-3} \pm 5x10^{-4}$	68

Fig. S1. FRAP of emerin in U2OS cells. (A) U2OS cells transfected with pA-TagRFP-emerin fusions after photoactivation and photobleaching of a circular region of interest at the nuclear envelope. Scale bar: 5 µm. (B) FRAP recovery curves of wild-type (WT), P183H, Q133H, and Δ95-99 mutated emerin at the nuclear envelope. Grey bars represent the standard deviation of the mean at each time points. n= 9-12 cells per condition. (C) Diffusion coefficients of wild-type and mutated emerin determined by fitting FRAP recovery curves with a two-components fit.

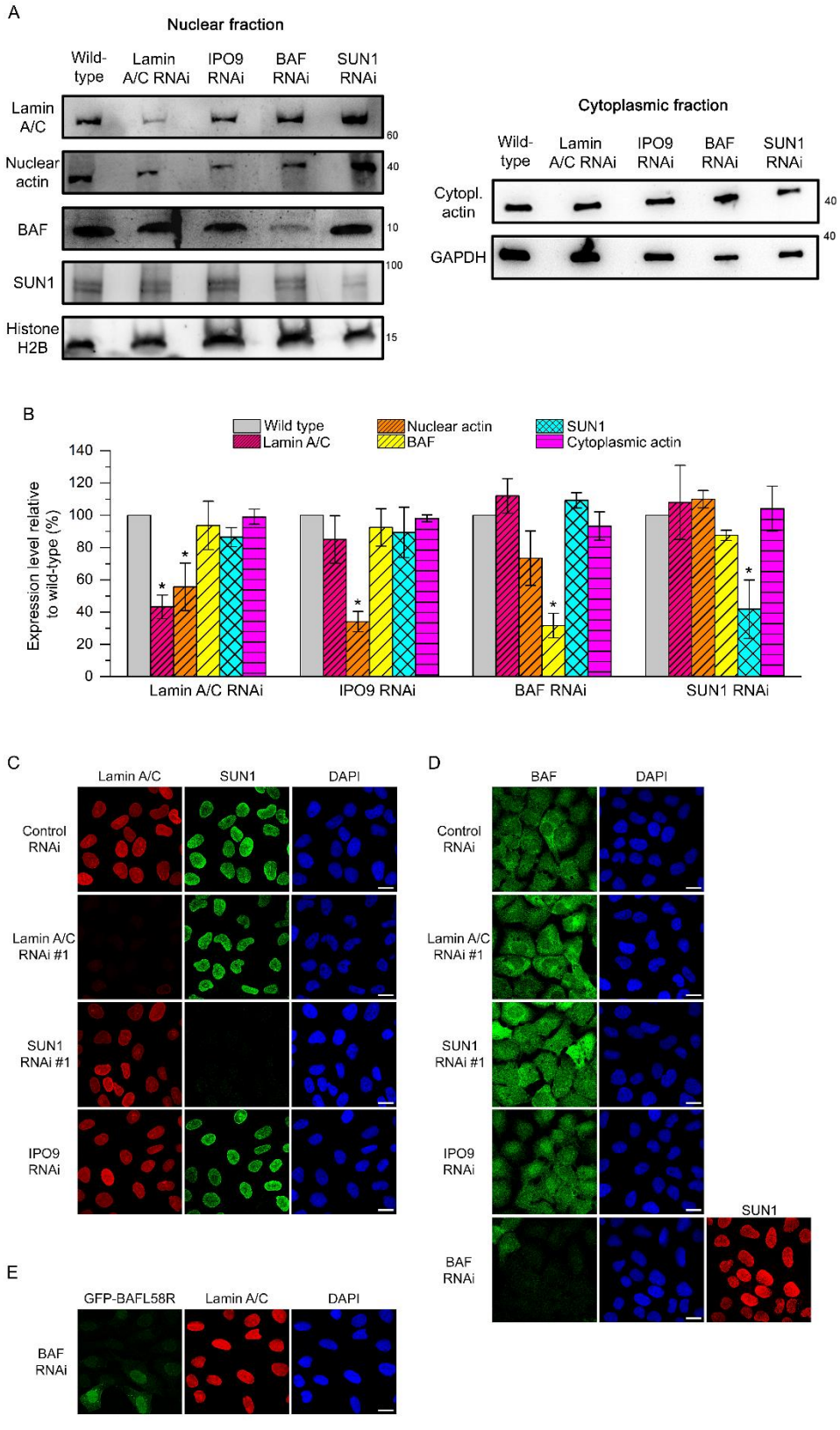

Fig. S2. Immunoblotting and immunostaining to assess the direct and indirect effects of siRNA knockdown against lamin A/C, IPO9, BAF and SUN1. (A) Western blots of lamin A/C, nuclear actin, BAF, SUN1 and histone H2A in the nuclear fraction (left) and of actin and GAPDH in the cytoplasmic fraction (right) of *EMD*$^{+/y}$ human dermal fibroblasts after RNA interference**.** (B) Relative change in lamin A/C, nuclear actin, BAF, SUN1 and cytoplasmic actin expression levels compared to untreated cells after siRNA **(**t-test, *: $p<0.05$**).** Error bars represent the standard deviation of the mean**.** (C) Confocal fluorescence imaging of lamin A/C, SUN1 and the nucleus (DAPI) after siRNA-induced depletion of lamin A/C, SUN1 and IPO9. All scale bars: 20 µm. (D) Confocal fluorescence imaging of endogenous BAF, the nucleus (DAPI) and SUN1 after siRNA-induced depletion of lamin A/C, SUN1, IPO9 or BAF. All scale bars: 20 µm. (E) Confocal fluorescence imaging of GFP-BAF^{L58R}, lamin A/C and the nucleus (DAPI) after siRNA-induced depletion of endogenous BAF. Scale bar: 20 µm.

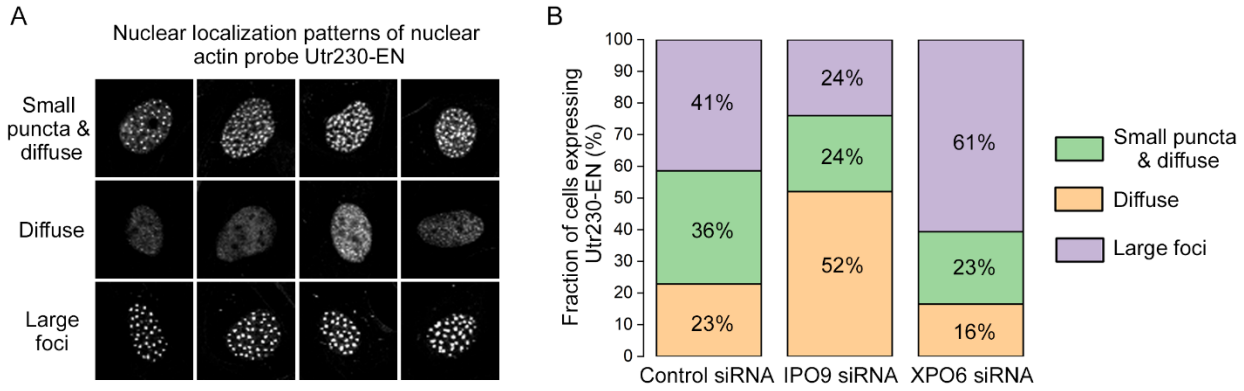

Fig. S3. Effects of IPO9 siRNA and XPO6 siRNA on nuclear actin organization. (A) Examples of nuclear localization patterns for the short nuclear actin filament probe Utr230-EN in HDF cells. Patterns are classified as: (i) small puncta and diffuse, (ii) diffuse or (iii) large foci, reflecting variations in nuclear actin filament content across cells. (B) Distribution of nuclear actin filament classes after control siRNA treatment (n = 635 nuclei), IPO9 siRNA (n = 663 nuclei) or XPO6 siRNA (n = 625 nuclei). Knockdown of IPO9 results in the majority of cells displaying a diffused Utr230-EN pattern, indicative of lower nuclear actin filament contents. Inversely, knockdown of XPO6 results in the majority of cells displaying larger and brighter foci compared to control siRNA, indicative of increased nuclear actin filament contents.

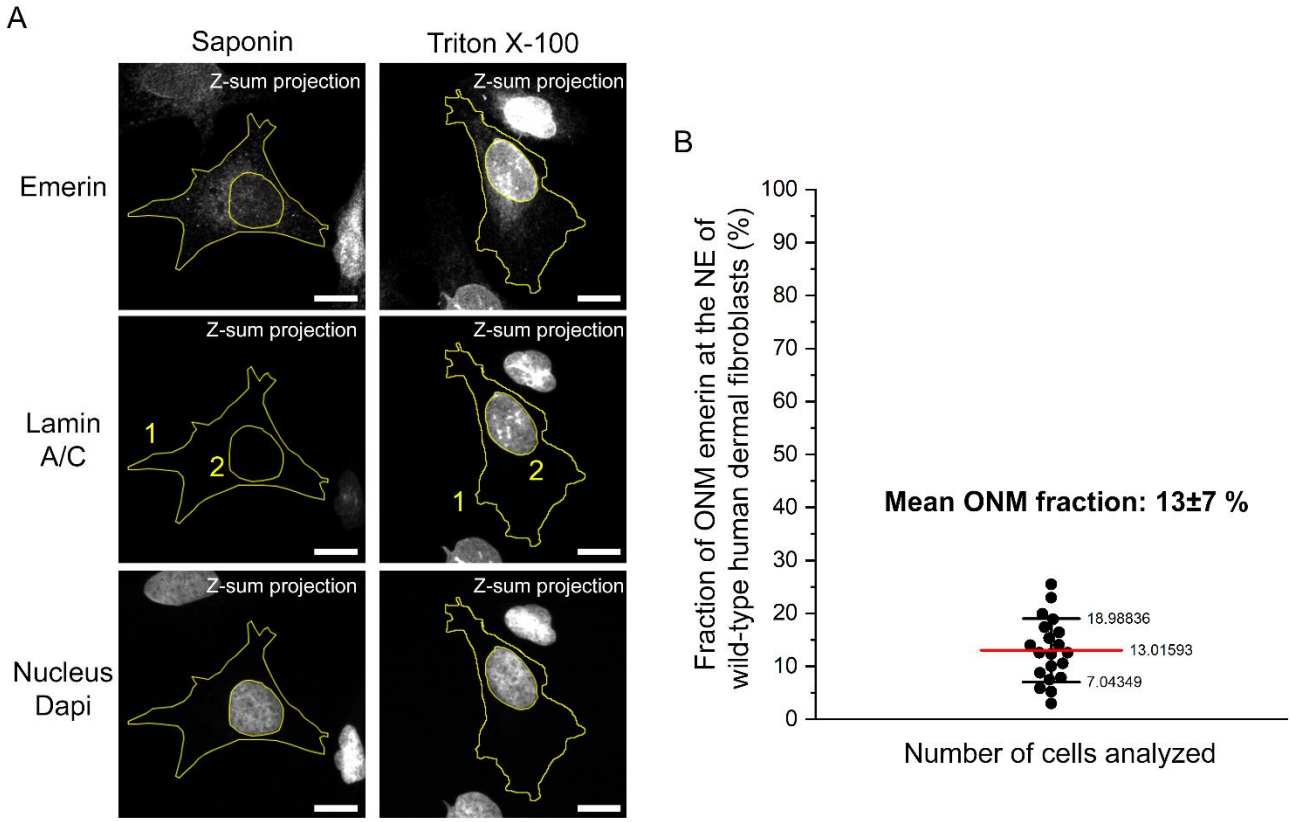

Fig. S4. Quantification of ONM emerin fraction in *EMD*$^{+/y}$ human dermal fibroblasts from confocal z-stacks. (A) Example of z-stack sum intensity projections for fibroblasts permeabilized with saponin or triton X-100 and immunostained for emerin, lamin A/C and Dapi. Region of interests (ROIs) used to measure fluorescence intensities from emerin immunostaining are shown in yellow. Scale bars: 15 µm. (B) Histogram of emerin ONM fraction at the nuclear envelope determined from confocal z-stack projections and nuclear ROI quantifications of saponin treated cells (N=20) and Triton X-100 treated cells (N=20). Mean is indicated by the red bar.

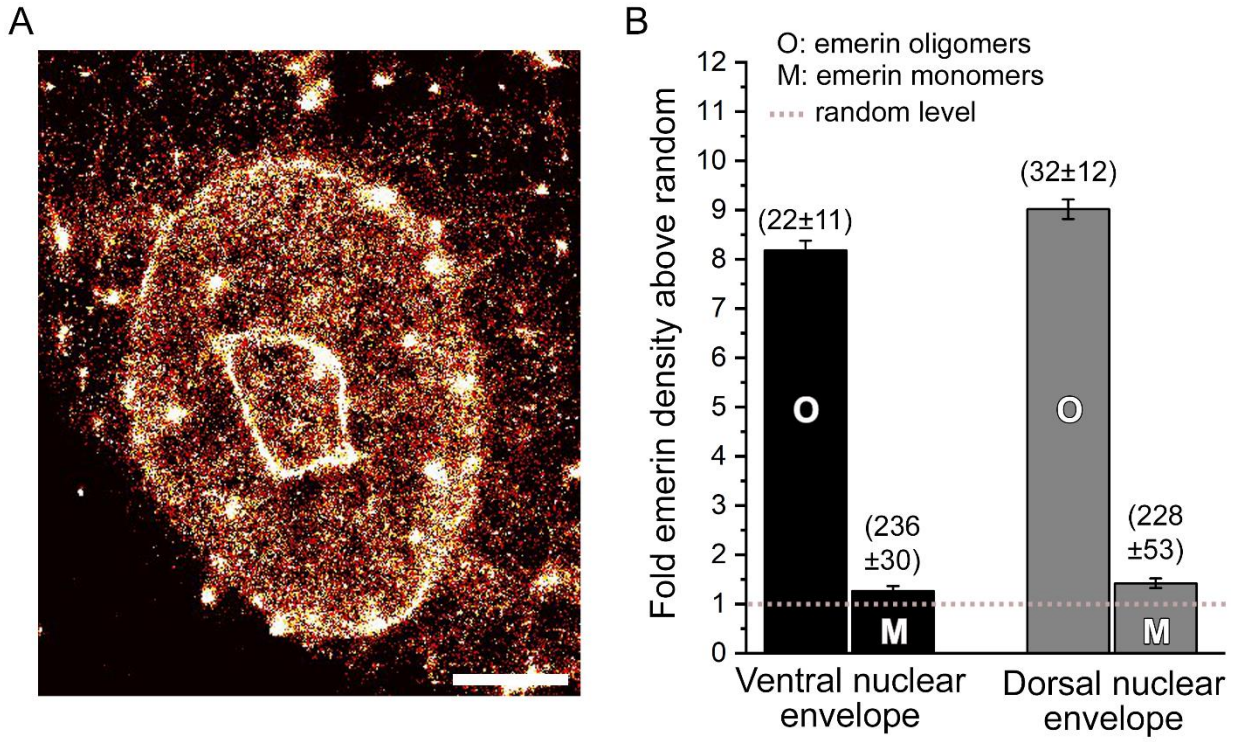

Fig. S5. Nanoscale organization of emerin at the dorsal nuclear envelope of human dermal fibroblasts. (A) Two-dimensional rendering of wild-type SNAP-emerin imaged by 3D super-resolution at the dorsal nuclear envelope. Areas with very high densities of emerin (white spots and lines) correspond to local nuclear envelope folds often observed in the plane of the dorsal nuclear envelope and to the 2D-projection of different z-positions of emerin at the nuclear rim. Scale: 5 µm. (B) Comparison of molecular densities above random (± s.e.m.) for wild-type emerin oligomers (O) and monomers (M) at the ventral (189331 localizations, 10 nuclei) or the dorsal (51387 localizations, 4 nuclei) nuclear envelope of human dermal fibroblasts. Values in parenthesis represent the size (± s.e.m.) of each domain in nanometers.

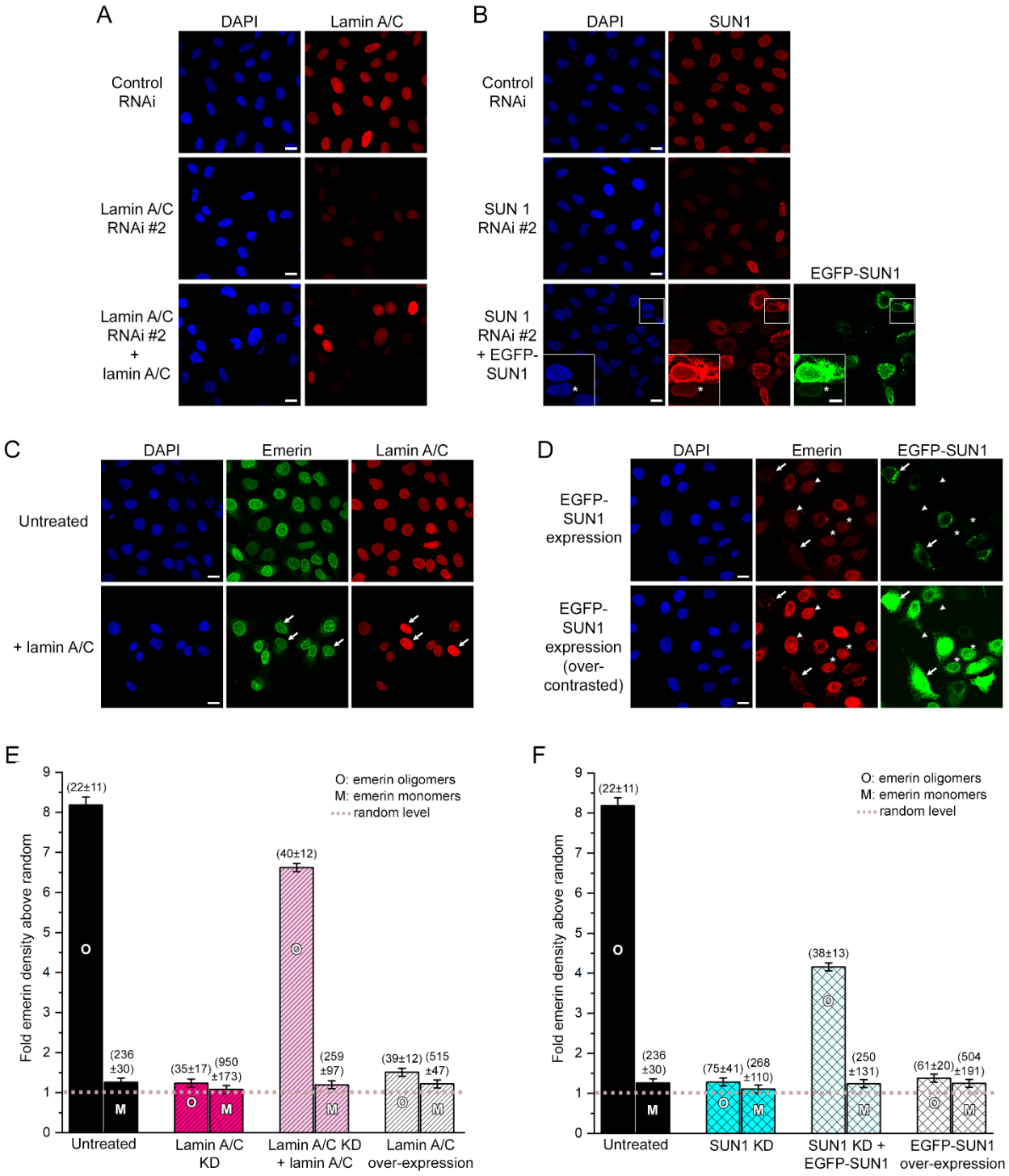

Fig. S6. Rescue by expression of exogenous lamin A/C or SUN1 after siRNA knock-down and effects of their over-expression on emerin localization and nanoscale organization. A) Confocal fluorescence imaging of lamin A/C and the nucleus (DAPI) after siRNA-induced depletion of lamin A/C and re-expression of exogenous and siRNA-resistant lamin A/C. Scales: 20 µm. B) Confocal fluorescence imaging of SUN1, EGFP-SUN1 and the nucleus (DAPI) after siRNA-induced depletion of endogenous SUN1 and re-expression of exogenous and siRNA-

resistant EGFP-SUN1. The over-contrasted inset shows that overexpression of EGFP-SUN1 induces the mis-localization of SUN1 from the nuclear envelope, while cells with low EGFP-SUN1 expression display relatively normal nuclear envelope accumulation (star). Scales: 20 µm, inset: 10 µm. C) Confocal fluorescence imaging of lamin A/C, emerin and the nucleus (DAPI) after overexpression of exogenous lamin A/C. Cells overexpressing lamin A/C (arrows) display an apparently normal emerin localization at the nuclear envelope. Scales: 20 µm. D) Confocal fluorescence imaging of emerin, EGFP-SUN1 and the nucleus (DAPI) after overexpression of exogenous EGFP-SUN1. EGFP-SUN1 overexpression induces a mis-localization of emerin from the nuclear envelope (arrows), while low EGFP-SUN1 expression levels (stars) result in relatively normal emerin localization at the nuclear envelope compared to non-expressing cells (arrowheads). Scales: 20 µm. (E) Molecular densities above random (± s.e.m.) for wild-type emerin in untreated cells, after lamin A/C knock down, lamin A/C knock down and exogenous expression of lamin A/C (118859 localizations, 6 nuclei) or overexpression of lamin A/C (204532 localizations, 5 nuclei). Values in parenthesis represent the size (± s.e.m.) of each domain in nanometers. (F) Molecular densities above random (± s.e.m.) for wild-type emerin in untreated cells, after SUN1 knock down (258300 localizations, 6 nuclei), SUN1 knock down and exogenous expression of EGFP-SUN1 (85210 localizations, 5 nuclei) or overexpression of EGFP-SUN1 (288522 localizations, 7 nuclei). Values in parenthesis represent the size (± s.e.m.) of each domain in nanometers.

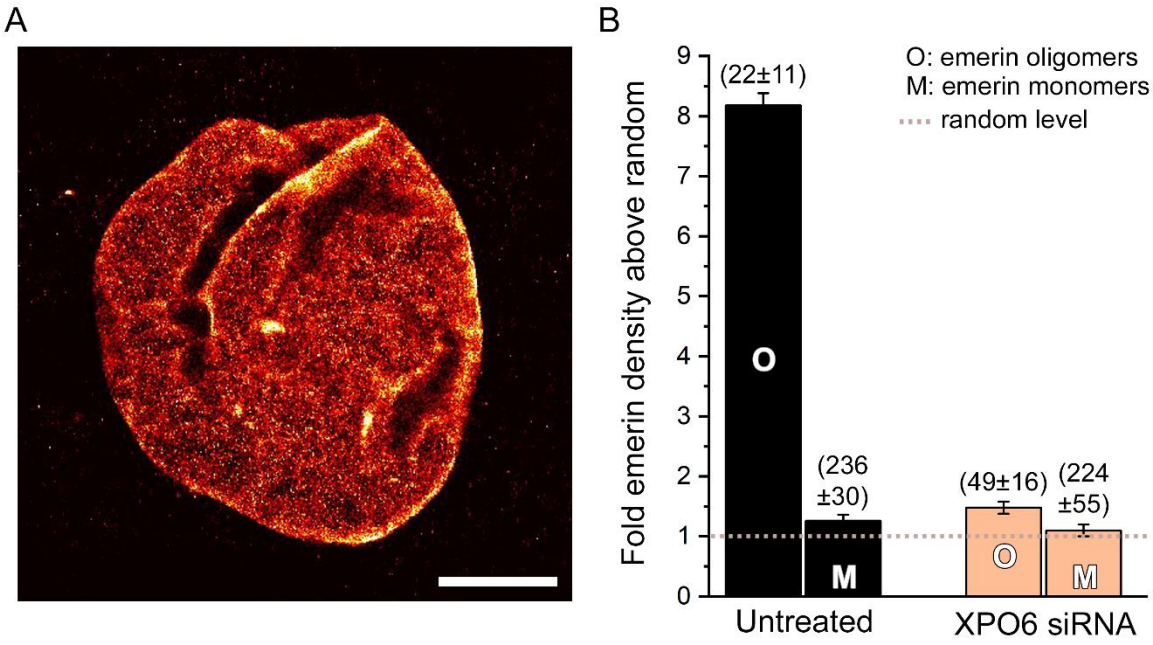

Fig. S7. Nanoscale organization of wild-type emerin following increase in nuclear actin levels by siRNA of exportin-6. (A) Two-dimensional rendering of wild-type SNAP-emerin imaged by 3D super-resolution in HDF cells treated with siRNA against exportin-6 (XPO6). Some nuclei appeared locally crumpled after siRNA of XPO6. Scale: 5 μm. (B) Molecular densities above random (± s.e.m.) for wild-type emerin oligomers (O) and monomers (M) in untreated cells or after XPO6 knock down to increase nuclear actin levels (315527 localizations, 7 nuclei). Values in parenthesis represent the size (± s.e.m.) of each domain in nanometers.

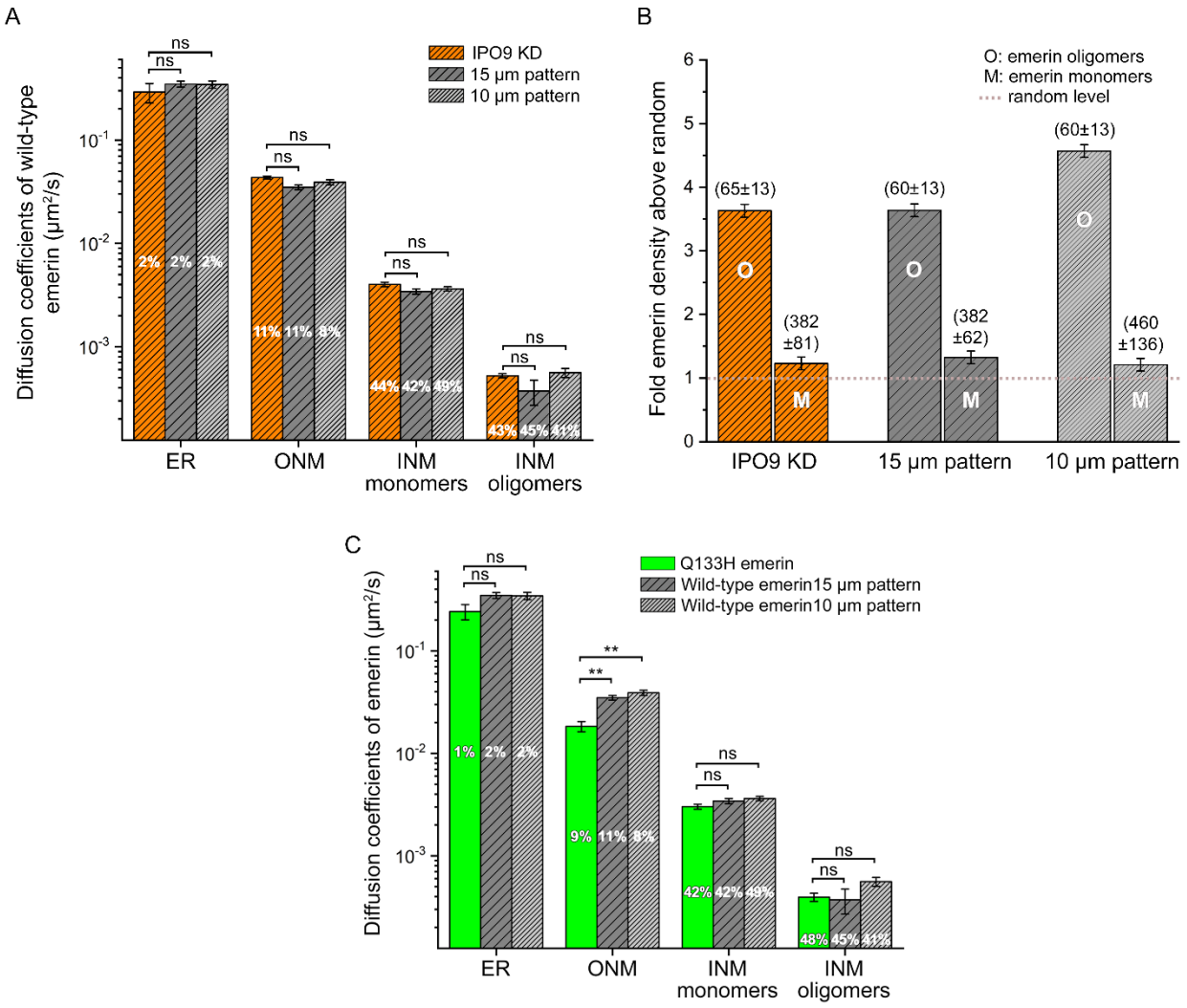

Fig. S8. Comparison of wild-type emerin organization after nuclear actin depletion or cell micropatterning and of Q133H and wild-type emerin diffusive behaviors. (A) Diffusion coefficients (± s.e.m.) and population percentage of wild-type emerin after nuclear actin depletion by IPO9 knock down (IPO9 KD, *n*=74501trajectories in 17 nuclei), after nuclear deformation on 15 µm wide (*n* *n*=27266 trajectories in 10 nuclei) or after nuclear deformation 10 µm wide micropatterns (*n*=12915 trajectories in 8 nuclei, t-test, ns: non-significant). (B) Relative nuclear envelope molecular densities above random (± s.e.m.) for wild-type emerin oligomers (O) and monomers (M) in non-patterned *Emd*$^{-/y}$ fibroblasts after nuclear actin depletion (IPO9 KD, n=225,394 localizations in 9 nuclei) and in micropatterned fibroblasts with deformed nucleus on 15 µm wide (n=151,647 localizations in 10 nuclei) or 10 µm wide micropatterns (n=56,563 localizations in 6 nuclei). Values in parenthesis represent the typical length size (± s.e.m.) of each domain in nanometers. (C) Comparison of Q133H emerin diffusion (± s.e.m.) and population percentage in non-patterned cells with that of wild-type emerin under mechanical stress on micropatterns (t-test, ns: non-significant, **: p<0.01).

Table S1. Diffusion coefficients of wild-type and mutated emerin determined by PDSD analyses after sptPALM or CALM imaging.

Emerin	D_1 (µm²/s)	D_2 (µm²/s)	D_3 (µm²/s)	D_4 (µm²/s)
Wild-type	$2.21x10^{-1}±4.9x10^{-2}$	$1.48x10^{-2}±1.5x10^{-3}$	$1.73x10^{-3}±1.1x10^{-4}$	$2.6x10^{-4}±1x10^{-5}$
Wild-type split-GFP complemented	not detected	$1.93x10^{-2}±2.5x10^{-3}$	not detected	$3.1x10^{-4}±5x10^{-5}$
Wild-type + lamin A/C knock down	$2.24x10^{-1}±6.1x10^{-2}$	$1.94x10^{-2}±1.9x10^{-3}$	$3.94x10^{-3}±4.1x10^{-4}$	$4.5x10^{-4}±3x10^{-5}$
Wild-type + IPO9 knock down	$2.91x10^{-1}±6.9x10^{-2}$	$4.34x10^{-2}±2.7x10^{-3}$	$4.01x10^{-3}±2.0x10^{-4}$	$5.2x10^{-4}±2x10^{-5}$
Wild-type + BAF L58R	$3.13x10^{-1}±5.3x10^{-2}$	$5.60x10^{-2}±1.4x10^{-3}$	$9.29x10^{-3}±9.3x10^{-4}$	$9.6x10^{-4}±6x10^{-5}$
Wild-type in 15 µm pattern	$3.48x10^{-1}±2.3x10^{-2}$	$3.49x10^{-2}±1.8x10^{-3}$	$3.43x10^{-3}±2.0x10^{-4}$	$3.7x10^{-4}±9x10^{-5}$
Wild-type in 10 µm pattern	$3.45x10^{-1}±2.8x10^{-2}$	$3.90x10^{-2}±2.3x10^{-3}$	$3.63x10^{-3}±1.8x10^{-4}$	$5.6x10^{-4}±5x10^{-5}$
Q133H	$2.42x10^{-1}±4.1x10^{-2}$	$1.83x10^{-2}±2.1x10^{-3}$	$3.02x10^{-3}±1.7x10^{-4}$	$3.9x10^{-4}±4x10^{-5}$
Δ95-99	$2.58x10^{-1}±1.1x10^{-2}$	$1.41x10^{-2}±1.3x10^{-3}$	$1.16x10^{-3}±0.6x10^{-4}$	$1.6x10^{-4}±1x10^{-5}$
P183H	$2.16x10^{-1}±2.1x10^{-2}$	$1.34x10^{-2}±1.8x10^{-3}$	$1.13x10^{-3}±1.3x10^{-4}$	$0.9x10^{-4}±2x10^{-5}$
P183H split-GFP complemented	$0.97x10^{-1}±1.6x10^{-2}$	$1.15x10^{-2}±3.0x10^{-3}$	$1.37x10^{-3}±1.8x10^{-4}$	not detected

Table S2. Molecular densities and domain sizes of wild-type and mutated emerin determined by spatial distribution analyses of emerin in super-resolved images.

Emerin	Oligomer density (fold above random)	Oligomer domain size (nm)	Monomer density (fold above random)	Monomer domain size (nm)
Wild-type	8.2±0.2	22±11	1.3±0.1	236±30
Wild-type + siRNA control	7.4±0.2	19±12	1.3±0.1	205±53
Wild-type + lamin A/C knock down	1.2±0.1	35±17	1.1±0.1	950±173
Wild-type + lamin A/C knock down + lamin A/C	6.6±0.1	40±12	1.2±0.1	259±97
Wild-type + lamin A/C overexpression	1.5±0.1	39±12	1.2±0.1	515±47
Wild-type + IPO9 knock down	3.6±0.1	65±13	1.2±0.1	382±81
Wild-type + XPO6 knock down	1.5±0.1	49±16	1.2±0.1	224±55
Wild-type + BAF L58R	2.0±0.1	85±19	1.3±0.1	718±250
Wild-type + SUN 1 knock down	1.2±0.1	75±41	1.1±0.1	268±110
Wild-type + SUN 1 knock down + EGFP-SUN1	4.2±0.1	38±13	1.2±0.1	250±131
Wild-type + EGFP-SUN1 over-expression	1.4±0.1	61±20	1.2±0.1	504±191
Wild-type + DN-KASH domain	1.2±0.1	61±20	1.1±0.1	393±119
Wild-type in 15 µm pattern	3.6±0.1	60±13	1.3±0.1	382±62
Wild-type in 10 µm pattern	4.6±0.1	60±13	1.2±0.1	460±136
Q133H	12.2±0.2	19±12	1.3±0.1	213±62
Δ95-99	1.3±0.1	48±14	1.1±0.1	420±51
P183H	2.2±0.1	35±12	1.3±0.1	321±29
Δ95-99 in 15 µm pattern	1.7±0.1	81±16	1.2±0.1	810±215
Δ95-99 in 10 µm pattern	2.0±0.1	75±20	1.2±0.1	499±250

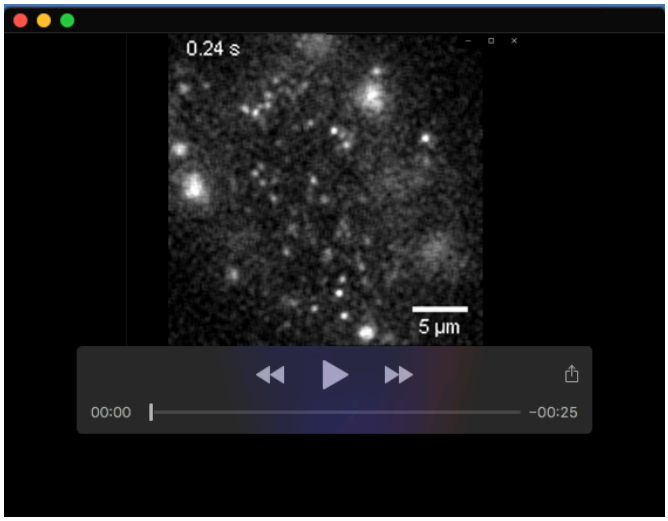

Movie 1. sptPALM imaging of wild-type PA-TagRFP-emerin at the nuclear envelope of an emerin-null dermal fibroblast (*Emd*$^{-/y}$). Point spread function have been intentionally expended to facilitate visualization. Movie acquired at 40 ms/frame and played back at the same rate.

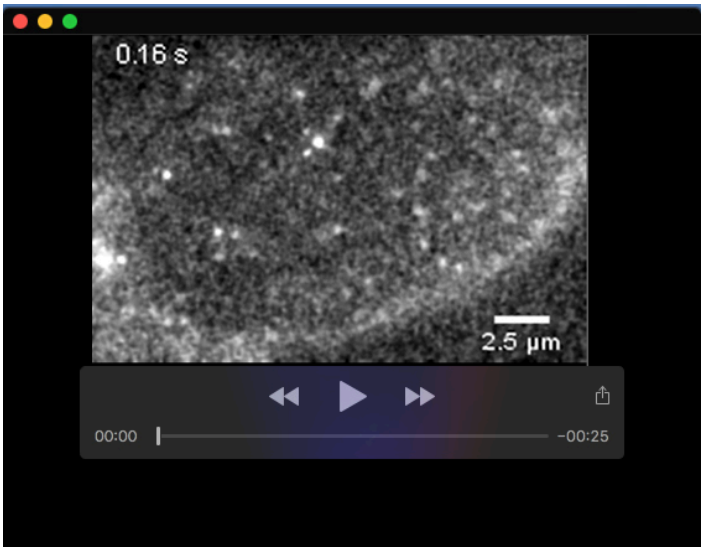

Movie 2. CALM imaging of complemented wild-type sGFP-emerin and M3-emerin dimers and oligomers at the nuclear envelope of an emerin-null dermal fibroblast (*Emd*$^{-/y}$). Movie acquired at 40 ms/frame and played back at the same rate.

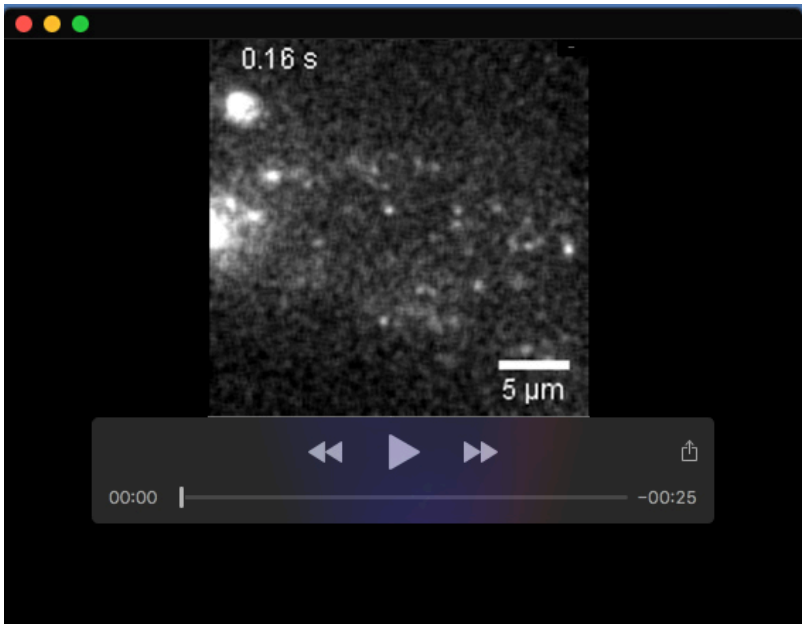

Movie 3. sptPALM imaging of wild-type PA-TagRFP-emerin at the nuclear envelope of an emerin-null dermal fibroblast (*Emd*$^{-/y}$) micropatterned on a 15 µm wide fibronectin strip. Movie acquired at 40 ms/frame and played back at the same rate.